Global and Planetary Change 199 (2021) 103433

Contents lists available at ScienceDirect

Global and Planetary Change

journal homepage: www.elsevier.com/locate/gloplacha

Research article

# Temperature reconstructions for the last 1.74-Ma on the eastern Tibetan Plateau based on a novel pollen-based quantitative method

Yan Zhao [a,b,*], Chen Liang [a,c], Qiaoyu Cui [a], Feng Qin [a], Zhuo Zheng [d], Xiayun Xiao [e], Chunmei Ma [f], Vivian A. Felde [g], Yaoliang Liu [a], Quan Li [a], Zhiyong Zhang [a], Ulrike Herzschuh [h], Qinghai Xu [i], Haicheng Wei [j], Maotang Cai [a], Xianyong Cao [k], Zhengtang Guo [b,l], H. John B. Birks [g,m]

[a] *Institute of Geographic Sciences and Natural Resources Research, Chinese Academy of Sciences, Beijing 100101, China*
[b] *University of Chinese Academy of Sciences, Beijing 100049, China*
[c] *Department of Land Resource and Urban Planning, Hebei GEO University, Shijiazhuang 050031, China*
[d] *Department of Earth Sciences, Sun Yat-sen University, Guangzhou 510275, China*
[e] *Nanjing Institute of Geography and Limnology, Chinese Academy of Sciences, Nanjing 210008, China*
[f] *School of Geography and Ocean Science, Nanjing University, Nanjing 210023, China*
[g] *Department of Biological Sciences and Bjerknes Centre for Climate Research, University of Bergen, Postbox 7803, N-5020 Bergen, Norway*
[h] *Periglacial Research Section, Alfred Wegener Institute, Helmholtz Centre for Polar and Marine Research, Telegraphenberg A43, 14473 Potsdam, Germany*
[i] *College of Resources and Environment Science, Hebei Normal University, Shijiazhuang 050024, China*
[j] *Key Laboratory of Salt Lake Resources and Chemistry, Qinghai Institute of Salt Lakes, Chinese Academy of Sciences, Xining 810008, China*
[k] *Institute of Tibetan Plateau Research, Chinese Academy of Sciences, Beijing 100101, China*
[l] *Key Laboratory of Cenozoic Geology and Environment, Institute of Geology and Geophysics, Chinese Academy of Sciences, Beijing 100029, China*
[m] *Environmental Change Research Centre, University College London, London WC16BT, UK*

ARTICLE INFO

*Keywords:*
Tibetan Plateau
Pollen
LW-WAPLS
Glacial-interglacial scale
Temperature variability

ABSTRACT

Terrestrial palaeo-temperature data are of great value in improving our understanding of past climate and they provide a basis for evaluating climate simulations. Such data are, however, poorly constrained for long time-scales. In addition to the scarcity of high-quality continuous time-series, finding proxies with a clear response to past temperature changes and developing appropriate reconstruction methods are major challenges. We present a new and robust method – Locally-weighted Weighted-average partial least squares (LW-WAPLS) to reconstruct quantitative temperature changes based on a high-resolution 1.74-Ma pollen record from the Zoige Basin on the eastern Tibetan Plateau, where the vegetation today is mainly controlled by temperature. The reconstructed mean annual (MAT) and warmest month (MTWM) temperatures reveal a general cooling trend with two major shifts at ~1.54 and 0.62 Ma BP, and regular glacial-interglacial variability ranging from ~ –4 to 2 °C and from 8 to 16 °C, respectively. They indicate ~4–5 °C (MAT) and ~ 5–6 °C (MTWM) magnitudes of glacial-interglacial temperatures. Both statistical and ecological evaluations validate the reliability of the reconstructions. The reconstructions provide important insights into the spatial aspects of long-term terrestrial temperature change. LW-WAPLS shows advantages over both the traditional modern analogue technique and non-linear transfer-function methodologies such as WAPLS for reconstructing the broad-scale climate changes for the Zoige Basin, by combining the strength of both methods. The LW-WAPLS approach potentially provides a robust tool to develop pollen-based climate reconstructions over long time-scales.

## 1. Introduction

Quantitative temperature reconstructions over long time-scales are of great value for understanding past climate dynamics and in providing insights into present and future climate warming. Available ice-core and marine records (e.g. Petit et al., 1999; Jouzel et al., 2007; Herbert et al., 2010; Snyder, 2016) provide an important framework for high-latitude air temperature and sea-surface temperature change at glacial-

* Corresponding author at: Institute of Geographic Sciences and Natural Resources Research, Chinese Academy of Sciences, Beijing 100101, China.
*E-mail address:* zhaoyan@igsnrr.ac.cn (Y. Zhao).

https://doi.org/10.1016/j.gloplacha.2021.103433
Received 9 August 2020; Received in revised form 26 December 2020; Accepted 20 January 2021
Available online 30 January 2021

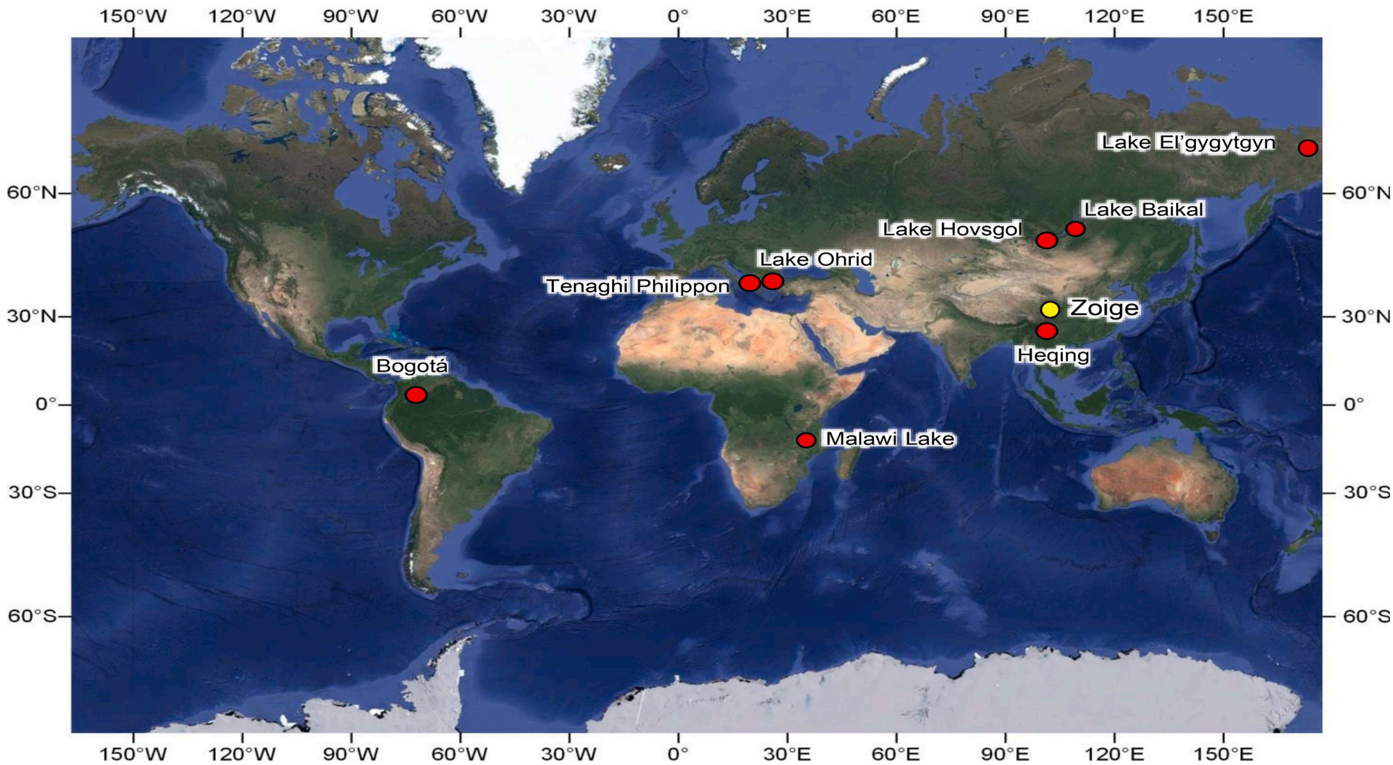


**Fig. 1.** Location map of the study site and other long records from lake sediments. They include: Zoige core ZB13-C2, this study, yellow dot; Lake El'gygytgyn (Melles et al., 2012; Brigham-Grette et al., 2013); Lake Baikal (Prokopenko et al., 2006); Tenaghi Philippon (Tzedakis et al., 2006); Lake Ohrid (Wagner et al., 2019); Lake Malawi, (Johnson et al., 2016); Bogotá Basin (Torres et al., 2013); and Heqing (An et al., 2011). (For interpretation of the references to colour in this figure legend, the reader is referred to the web version of this article.)

interglacial scales, such as the Middle Pleistocene Transition, the larger magnitude of interglacials after the Mid-Bruhnes Event, and millennial abrupt changes.

Terrestrial long-term archives with reasonable temporal resolution are, however, very scarce. Available records with an average resolution of $<2000$ years (see Fig. 1) include: the 3.6-Ma XRF and pollen record (but restricted to several interglacials during the Quaternary) from Lake El'gygytgyn (Melles et al., 2012; Brigham-Grette et al., 2013); the 1.8-Ma biogenic silica record from Lake Baikal (Prokopenko et al., 2006); the 1.35-Ma pollen record from Tenaghi Philippon (Tzedakis et al., 2006); the 1.36-Ma pollen and total organic carbon records from Lake Ohrid (Wagner et al., 2019); the 1.3-Ma $TEX_{86}$, Ca, and leaf wax $\delta^{13}C_{31}$ records from Malawi Lake (Johnson et al., 2016); the 2.5-Ma pollen record from the Bogotá Basin (Torres et al., 2013); and the 2.6-Ma Rb/Sr ratio, TOC, and *Tsuga* pollen records from Heqing Paleolake in southwestern China (An et al., 2011). The oldest loess sequence in China dates back to ~22 Ma (Guo et al., 2002), and there are a number of grain-size, magnetic susceptibility, and $Fe_t/Fe_d$ ratio records from loess sections that cover the Quaternary (e.g. Guo et al., 2000; Ding et al., 2002). Few of these records provide temperature reconstructions. Melles et al. (2012) and Brigham-Grette et al. (2013) present temperature reconstructions for the Lake El'gygytgyn region, but the reconstructions are restricted to 3.6–2.2 Ma and to some interglacials over the past 2.2 Ma based on the best analogue method (BAM) and pollen data. At Lake Malawi, a continuous terrestrial temperature record spanning the past 1.3 Ma was reconstructed from the $TEX_{86}$ record. Chevalier et al. (2020a) recently reconstructed the temperature changes of southeastern Africa over the past 790 ka using the Bayesian method CREST (Climate REconstruction SofTware) based on pollen assemblages from a marine core (with a coarse resolution of 3–6.7 ka). A scarcity of high-quality continuous terrestrial quantitative palaeoclimate records has greatly hampered the investigation of global and regional features at glacial-interglacial time-scales and hence evaluating climate simulations to help understand long-term climate dynamics.

In addition to the scarcity of high-quality continuous geological time-series, finding proxies with a clear temperature signal and appropriate reconstruction methods is a major challenge. Pollen has been long recognized as a powerful proxy used for quantitative climate reconstructions (e.g. Webb and Bryson, 1972). Previous studies for the period since the Last Glacial Maximum (LGM) have demonstrated that the quality of the modern pollen training-set, the sensitivity of vegetation to climate variables, and the selection of appropriate numerical approaches, are critical for robust climate reconstructions (Birks et al., 2010; Chevalier et al., 2020b). Various techniques have been widely applied in pollen-based palaeoclimate reconstructions (Birks et al., 2010; Chevalier et al., 2020b). These include presence-only distribution data based on the indicator-species approach (e.g. Probability Density Functions; Kühl et al., 2002, 2007; Chevalier et al., 2020a, 2020b), multivariate transfer-functions (e.g. WA/WA-PLS; Birks et al., 1990a, 2010), and the modern analogue technique (Overpeck et al., 1985; Guiot, 1990). Recent advances in computation and efficient algorithms allow a Bayesian approach, defined using conditional probability distributions (Chevalier et al., 2020b). Such approaches are becoming more easily applicable (e.g. Haslett et al., 2006; Holden et al., 2017). An inverse-vegetation modelling approach, which considers various environmental conditions such as lowered atmospheric $CO_2$ concentrations, has been developed and used to reconstruct climate in Europe, Africa, and North America (e.g. Guiot et al., 2000; Wu et al., 2007a, 2007b; Izumi and Bartlein, 2016). All techniques have their own set of advantages and limitations (Birks et al., 2010; Chevalier et al., 2020b). For example, due to the large-magnitude temperature changes over glacial-interglacial cycles, the commonly used traditional multivariate transfer-function approach can produce large uncertainties due to problems such as edge effects and overfitting (Birks et al., 2010). Instead, the modern analogue technique, also known as the best analogue method (BAM), is widely used for many records spanning the LGM and longer time-series (e.g. Melles et al., 2012; Brigham-Grette et al., 2013). However, the modern analogue technique often encounters spatial autocorrelation problems, leading to over-optimistic prediction errors (Juggins and Birks, 2012; Telford and Birks, 2005; Birks et al., 2010). It may also tend to produce noisy or "spiky" reconstructions with a small number of analogues, or flat profiles with a large number of analogues, which may damp out fine-scale variation (Birks et al., 2010; Juggins and Birks, 2012). Another major limitation of the modern analogue method is the occurrence of "no-analogue" assemblages in the past. Therefore, multiple techniques should be examined for selecting the most appropriate approach, due to differences in training-set size, temporal and spatial scales of study, research questions, taxonomic diversity, and the form and complexity of species-environment relationship (Birks et al., 2010; Juggins and Birks, 2012; Chevalier et al., 2020b).

The Tibetan Plateau is one of the key regions for filling the long-term palaeoclimatic data gap, as its thermal effect plays a crucial role in modulating Asian monsoons, arid environments in Central Asia, and even global climate (Dallmeyer et al., 2011; Abe et al., 2013; Wu et al., 2015). We present a 1.74-Ma high-resolution pollen sequence from the Zoige Basin in the eastern Tibetan Plateau, whose vegetation today is very sensitive to temperature variability. We developed a novel and robust approach - LW-WAPLS (Locally-weighted Weighted-average partial least squares) to derive quantitative temperature estimates. The multi-proxy (including pollen) data and temperature reconstructions are briefly presented by Zhao et al. (2020), which focus on the spectral features of the reconstructed orbital-suborbital climate change and its dynamics. Here, we present and discuss the detailed quantitative reconstruction approach and evaluations of the reconstructions. Our objectives are to: (1) assess the robustness of LW-WAPLS based on comparisons with other related approaches and the critical evaluation of the results; (2) provide a high-resolution temperature sequence for the Tibetan Plateau over the past 1.74 Ma; and (3) briefly discuss the latitudinal gradients of the magnitude of the temperature changes at glacial-interglacial scales.

## 2. Materials and methods

### 2.1. Study region

The Zoige Basin is located on the eastern Tibetan Plateau (Fig. 1; Supplementary (S) Fig. 1). Mean annual temperature at the Maqu and Zoige meteorological stations within the basin is ~1.4–1.8 °C (based on data from 1981 to 2010 downloaded from China Meteorological Administration: http://data.cma.cn) (Supplementary (S) Table S1). July (the warmest month) temperature is ~10.8 °C and January (the coldest month) temperature is $\sim -10.2$ °C. The below-zero season is from November to March. Mean annual precipitation is about 600–650 mm. As the Zoige Basin is heavily influenced by the Asian monsoon, most precipitation falls as rain during the summer months (Fig. S1) and thus temperature and precipitation are highly correlated (Fig. S2).

The Zoige Basin is presently covered by alpine meadows dominated by *Kobresia* spp. and related taxa. The surrounding mountains support scattered forests up to ~4000 m above sea level (a.s.l.), mainly composed of *Picea asperata*, *P. wilsonii*, *P. purpurea*, *Abies faxoniana*, *Pinus densata*, *Betula platyphylla,* and *Quercus liaotunggensis*, and by shrubs, mainly *Salix* spp. and *Rhododendron* spp. (Hou, 2001; Shen et al., 2005). Temperature is the dominant climate control for these major vegetation types in this forest-alpine meadow ecotonal area (Shen et al., 2003; Zhao et al., 2011; Fig. S1).

### 2.2. Fossil pollen record

A 573.39 m-long sediment core ZB13-C2 (33°58.163′N, 102°19.855′E, 3434 m a.s.l) was retrieved in 2013 from the Zoige Basin (Zhao et al., 2020), which finally dried out at ~30 ka BP due to river capture by the Yellow River (Chen et al., 1999). Orbitally-tuned

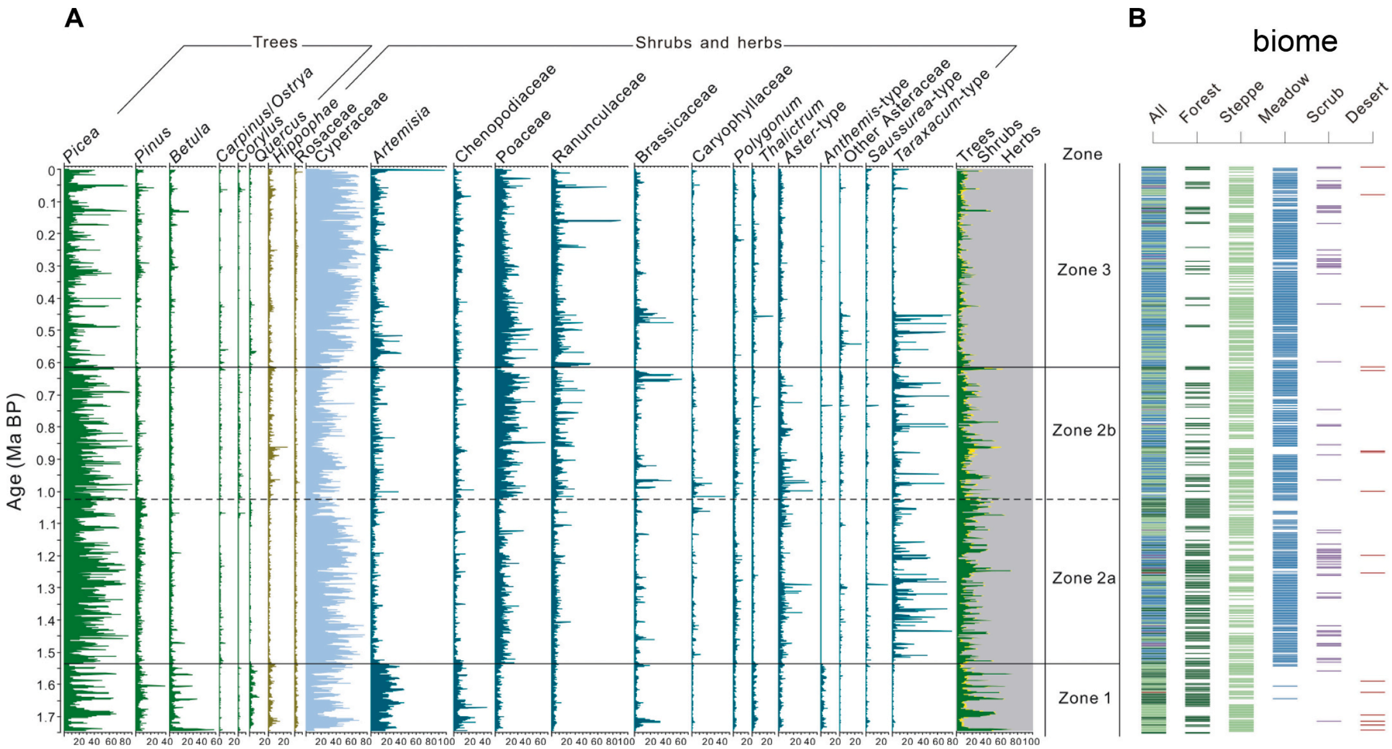


**Fig. 2.** Pollen percentage diagram of the major taxa and biome reconstruction from the Zoige Basin core ZB13-C2 (from Zhao et al., 2020). A. Pollen percentage diagram. The pollen zonation is based on CONISS results aided by a multivariate regression tree analysis, which shows the biggest assemblage changes at 1.54 Ma BP and 0.62 Ma BP. B. Combined biome reconstruction.

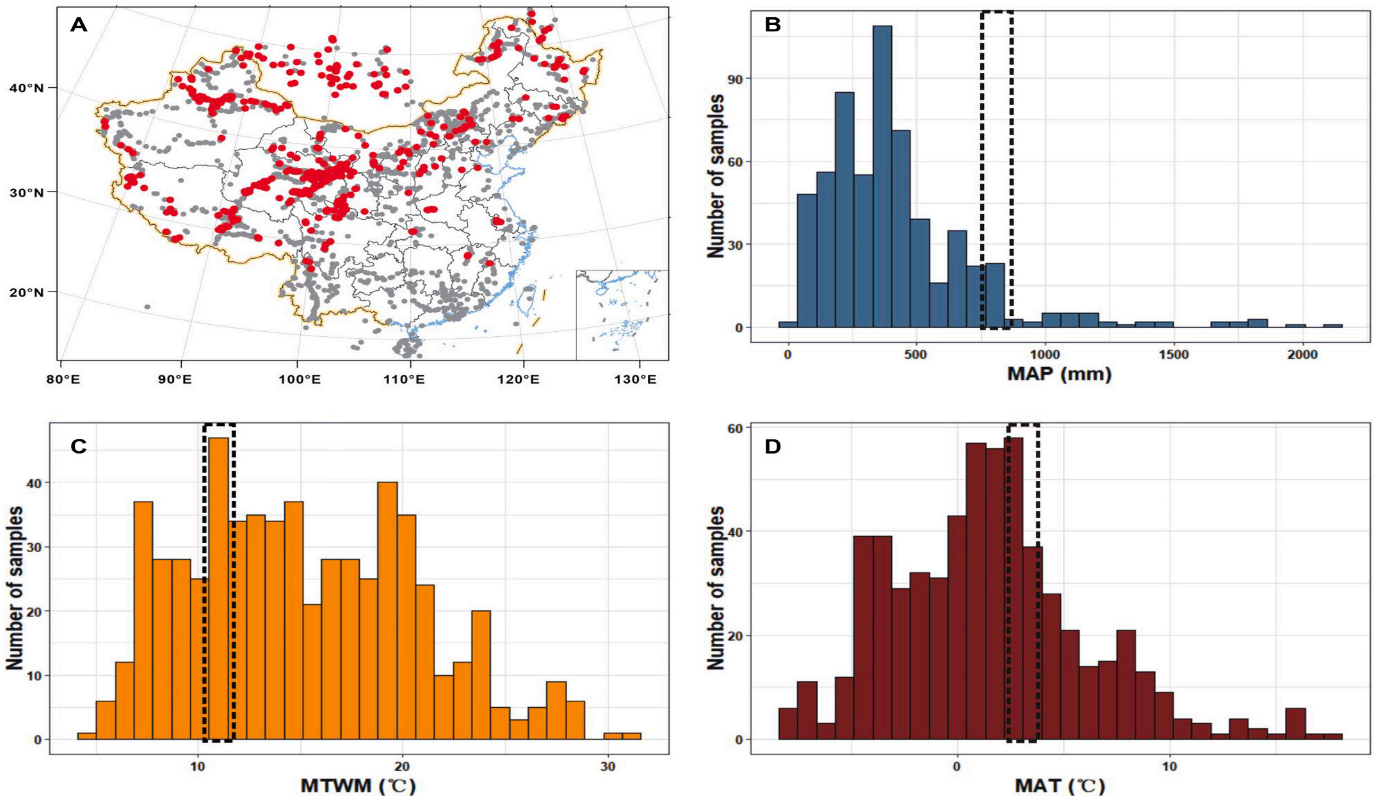


**Fig. 3.** Distribution of the samples in the modern pollen training-sets. A. All the modern pollen sites (grey dots) and analogue training sites (red dots). B Mean annual precipitation (MAP), C mean temperature of warmest month (MTWM), and D mean annual temperature (MAT) distribution patterns of the calibration-set selected for LW-WAPLS and the modern meteorological observations in the study region (black dashed line). (For interpretation of the references to colour in this figure legend, the reader is referred to the web version of this article.)

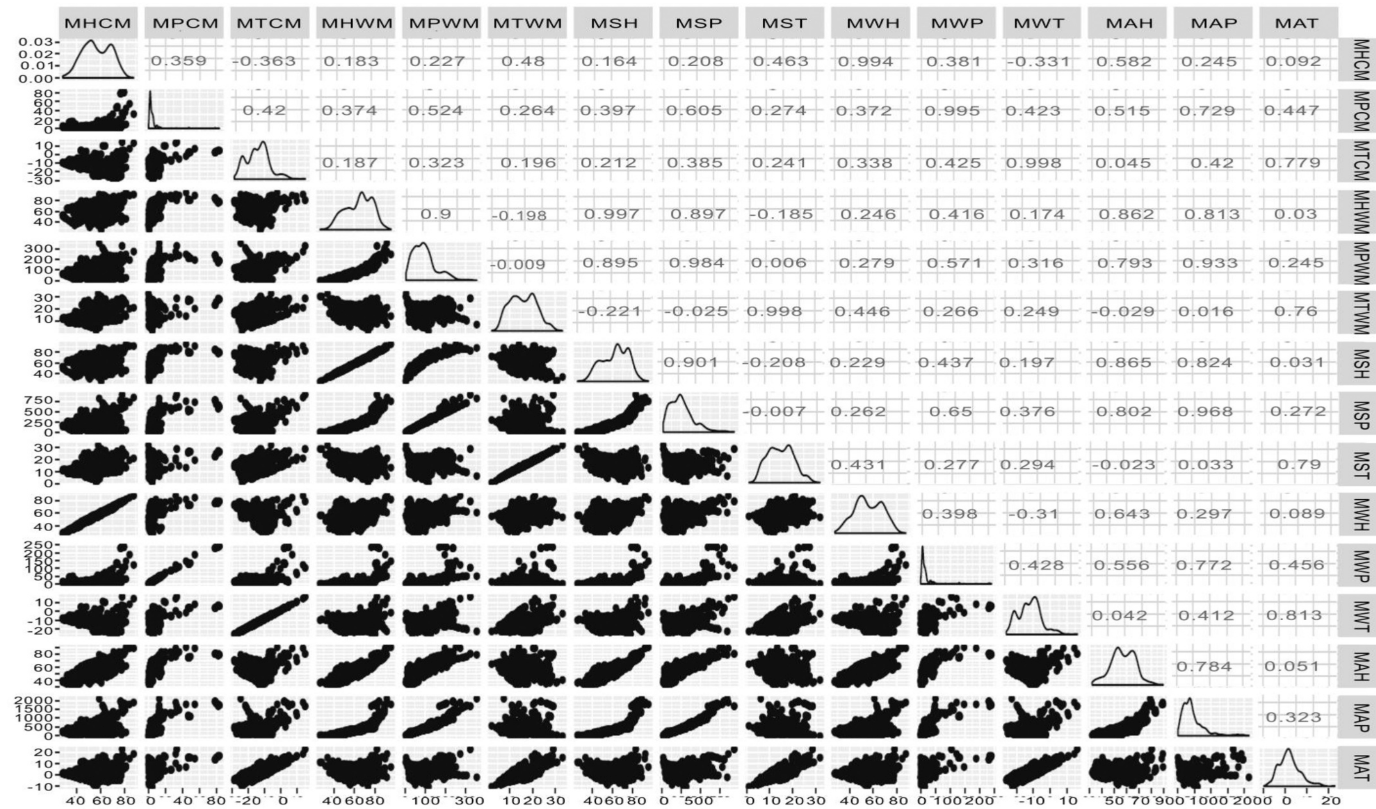


**Fig. 4.** Correlation analysis of climate variables. M: mean; T: temperature; H: humidity; S: summer; A: annual; WM: warmest month; CM: coldest month. 6 major variables include: MTCM = mean temperature of coldest month; MTWM = mean temperature of warmest month; MAT = mean annual temperature; MPCM = mean precipitation of coldest month; MPWM = mean precipitation of the warmest month; MAP = mean annual precipitation.

**Table 1**
Summary statistics for Variance Inflation Factors (VIF) with 6 variables and the explained variance of each climate variable as the sole predictor for samples in the training-set using canonical correspondence analysis (CCA).

| Climate variables | VIF Run1 (all variables) | VIF Run2 (without MTWM) | VIF Run3 (without MTCM) | VIF Run4 (4 variables) | Climatic variables as sole predictor | |
|---|---|---|---|---|---|---|
| | | | | | Explained variance | *p*-value |
| MPCM | 4.87 | 3.54 | 3.79 | 2.30 | 2.03 | 0.005 |
| MPWM | 15.85 | 14.63 | 15.00 | – | 2.79 | 0.005 |
| MAP | 28.05 | 21.59 | 23.19 | 2.32 | 2.64 | 0.005 |
| MTCM | 57.16 | 7.64 | – | – | 3.85 | 0.005 |
| MTWM | 45.66 | – | 3.31 | 3.14 | 5.21 | 0.005 |
| MAT | 119.58 | 7.71 | 3.26 | 3.17 | 5.07 | 0.005 |

Notes: Runs 1–4 illustrate the process of variable selection. Run 1: with all variables; Run 2: without MTWM; Run 3: remove MTCM; Run 4: remove MTCM, MPCM, and MPWM.
MPCM: mean precipitation of coldest month. MPWM: mean precipitation of warmest month. MAP: mean annual precipitation. MTCM: mean temperature coldest month. MTWM: mean temperature of warmest month. MAT: mean annual temperature.

timescales, with palaeomagnetic, radiocarbon (AMS $^{14}C$), and luminescence (OSL) dating controls, date the base of the core at ~1.74 Ma BP (Zhao et al., 2020).

A total of 2787 pollen sub-samples of ~2–8 $cm^3$ volume were taken at ~20-cm intervals. The temporal resolution is ~600 yr. Laboratory treatments are described in Zhao et al. (2020).

A summary percentage pollen diagram (Fig. 2) is shown and briefly described in Zhao et al. (2020). The entire pollen sequence is dominated by *Picea,* along with *Pinus*, *Betula*, and *Quercus,* and meadow/steppe taxa such as Cyperaceae, Asteraceae, *Artemisia,* and Poaceae. The percentage pollen diagram is divided into 3 pollen-assemblage zones, with subzones when necessary, based on a stratigraphically constrained hierarchical cluster analysis (CONISS) aided by multivariate regression trees (MRT) (Zhao et al., 2020; Fig. 2).

Zone ZB-1 (1.74–1.54 Ma BP; 573.39–493.7 m): The pollen assemblages are marked by conifer and deciduous mixed forest taxa (mostly *Picea* with percentages up to 68%, along with *Pinus*, *Betula*, and *Quercus*) during interglacials and steppe taxa (dominated by *Artemisia*) during glacial times. This zone has the highest percentages of *Artemisia* and deciduous tree pollen throughout the core.

Zone ZB-2 (1.54–0.62 Ma; 493.7–215.6 m): Assemblages shift between conifer forest during interglacials and meadow (dominated by Cyperaceae and steppe taxa) during glacials. The two subzones are delimited based mostly on increasing abundances of steppe taxa (mainly Poaceae and Ranunculaceae) at ~1.03 Ma BP.

Zone ZB-3 (0.62–0 Ma BP; 215.6–0 m): Over the last 0.62 Ma, the percentages of tree taxa greatly decrease. A less prominent change is observed at ~0.41 Ma BP after which *Taraxacum*-type and Poaceae pollen percentages decline.

### 2.3. Modern pollen data-set

The modern pollen data-set used for the quantitative reconstruction comprises 5405 samples across China and part of Mongolia (location see Fig. 3A), including 1756 samples derived from the East Asian Pollen Database (Zheng et al., 2008), 1387 new samples (unpublished data; Table S2), and 2272 from Herzschuh et al. (2019). Most modern samples come from surface soils (3382 samples), surface lake-sediments (680 samples), or moss-polsters (1112 samples).

To obtain a high-quality training-set or calibration-set, we first deleted 144 samples with <100 grains pollen counts and 94 samples from strongly human-disturbed vegetation types such as by cultivated areas. We then excluded 36 potential outliers identified using hierarchical cluster (H-cluster) analysis. We used 85% of the abundance extremes of rare pollen taxa as a threshold (see Fig. S3). We further excluded 253 samples from air-traps and dust-flux collectors because their pollen assemblages are potentially biased due to their different taphonomies and complex depositional processes, which is supported by their high RMSE (root mean square error) as estimated by leave-one-out cross validation. The remaining 4878 samples form the basis for our quantitative reconstruction.

In order to estimate the modern climate at the sites of the 4878 modern samples, we applied thin plate spline regression (Hijmans et al., 2005) to interpolate the modern climate data from 756 stations across China for the interval of 1981–2010 (http//:data.cma.cn) (Table S1), using the R package Fields (Nychka et al., 2020).

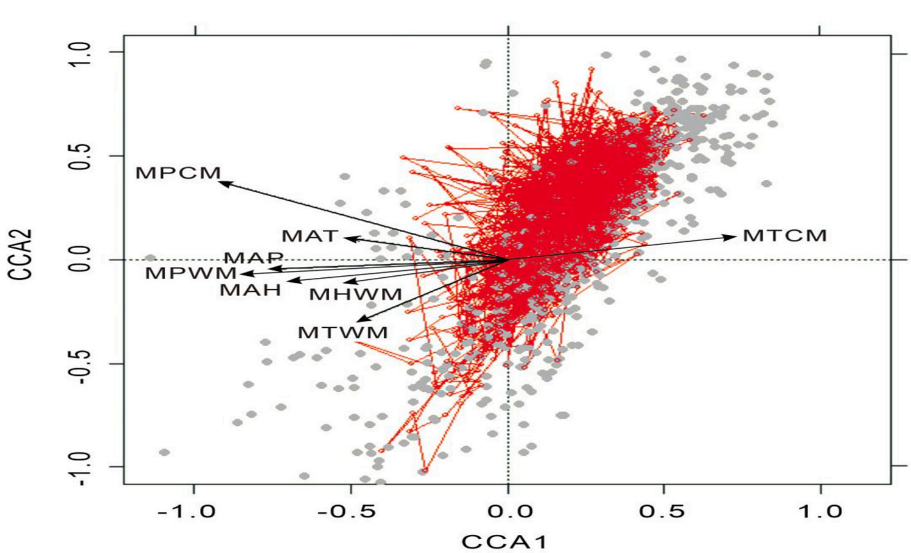


**Fig. 5.** Time-track analysis based on canonical correspondence analysis (CCA). The CCA shows the relationships between the modern training-set samples (grey dots) and four climate variables – mean precipitation of the coldest month (MPCM), mean annual temperature (MAT), mean annual precipitation (MAP), and mean temperature of the warmest month (MTWM). The fossil samples (red dots) were projected passively onto the CCA. (For interpretation of the references to colour in this figure legend, the reader is referred to the web version of this article.)

**Table 2**
Error estimates of mean annual temperature (MAT, °C), mean temperature of the warmest month (MTWM, °C), and mean annual precipitation (MAP, mm) for locally-weighted weighted-average partial least squares (LW-WAPLS) model using various numbers of analogues. Model errors are given as root mean square error of prediction (RMSEP) estimated by leave-one-out cross-validation.

| Variables | RMSEP_10 analogues | RMSEP_20 analogues | RMSEP_30 analogues | RMSEP_40 analogues | RMSEP_50 analogues |
|---|---|---|---|---|---|
| MAT | 3.35 | 3.43 | 4.08 | 4.25 | 4.41 |
| MTWM | 3.06 | 3.06 | 3.15 | 3.17 | 3.21 |
| MTCM | 3.51 | 3.32 | 3.99 | 4.06 | 4.43 |
| MAP | 158.05 | 169.62 | 157.00 | 160.39 | 160.4 |

### 2.4. Assessment of the critical climate forcing variable(s)

We applied several numerical methods to assess the critical climate forcing variable(s) for both the modern pollen and fossil pollen data (Juggins, 2013; Chevalier et al., 2020b). Pearson correlation coefficients between the climate variables for the 597 modern analogue samples were used to identify collinearity relationships among variables (Juggins and Birks, 2012). Variance inflation factors (VIFs) derived from canonical correspondence analysis (CCA) were used to remove those variables showing high multicollinearity until the VIF value was low (Ter Braak and Verdonschot, 1995). The relative contribution of each climate variable was estimated by the ratio ($\lambda_1$,/$\lambda_2$) of the constrained eigenvalue ($\lambda_1$) to the first unconstrained eigenvalue ($\lambda_2$) in the CCAs (Ter Braak, 1988). The variables making a small numerical contribution were progressively removed (Ter Braak and Verdonschot, 1995; Cao et al., 2014).

The Spearman coefficient for mean annual precipitation (MAP) vs. the warmest month precipitation (MPWM) is 0.933, indicating a strong monotonic relationship (Fig. 4). Therefore, MPWM was not used for reconstruction because of this strong co-linearity and its dominant contribution to MAP. MPCM was not included in the subsequent analysis in light of its limited numerical contribution and unclear ecological significance in the study region.

The VIF results indicate that MAT, MTWM, and MTCM contain much co-varying information (Table 1). When MTWM is removed, the VIF value of MTCM still exceeds 7.64. In contrast, the VIF value of MTWM is only 3.31 without MTCM. In addition, when the explained variance of the climatic variables is regarded as a sole predictor ($\lambda_1/\lambda_2$), MAT and MTWM show a better performance than any other variable (Table 3). Therefore, compared with MTCM, MTWM has a lower collinearity with MAT and thus potentially more explanatory power for the modern pollen data.

In order to illustrate the possible changes of the critical climate variables through time, a time-track analysis (Birks et al., 1990b; Juggins and Birks, 2012), was made based on the composition of the fossil samples and the modern taxon scores. The fossil samples were projected passively onto the underlying CCA modern ordination axes. The time-track of the sediment-core samples within the CCA reflects compositional similarities between the modern and fossil samples in relation to changes in the constraining climate variables (Birks et al., 1990b). The time-track plot indicates that the fossil pollen samples mostly fall parallel to the MTWM gradient and partly along the MAT gradient (Fig. 5), suggesting that the warmest month temperature (MTWM) is the main driver of long-term vegetation change at Zoige. Although mean precipitation of the coldest month (MPCM) and mean annual precipitation (MAP) have long biplot arrows (Fig. 5), we do not consider them to be the main drivers of long-term change for ecological reasons as explained below.

The assessment process so far is based purely on regional statistical indicators. As Chevalier et al. (2020b) emphasize, ecological aspects should also be considered. The modern vegetation in the eastern Tibetan Plateau is strongly influenced by the Asian summer monsoon. A stronger monsoon with a warmer and moister climate would cause an expansion of tree populations. However, in the alpine Zoige region, where moisture availability is relatively high, the density and elevational limits of forests are primarily controlled by temperature (Shen et al., 2005), particularly summer temperature, as cold-tolerant species (e.g., *Picea*, *Abies,* and other alpine taxa) are able to tolerate winters (frozen season) in this region. This is confirmed by the distinct elevational distribution of modern vegetation (see Fig. S1). Over long timescales, variations of the AP% in the core may mostly be a reflection of changes in temperature, particularly summer (growing season) temperature.

In summary, MTWM is considered to be the most appropriate climate variable for the final reconstruction on both statistical and ecological criteria. However, MAT, MTWM, and possibly MTCM contain much co-varying information, and reconstructions for individual variables may provide additional annual or seasonal perspectives.

### 2.5. Reconstruction model establishment

Multivariate calibration-function approaches (e.g. WA and WAPLS) and the modern analogue technique are commonly used for climate reconstructions based on fossil pollen percentage data. Multivariate calibration-function approaches assume either a linear or unimodal species-environment response and are inverse regression and calibration procedures (Birks et al., 2010; Juggins and Birks, 2012). WA and WAPLS assume a unimodal species–environment response. They are relatively robust to spatial autocorrelation (Telford and Birks, 2005). They generalize species–environment relationships well from moderately sized data-sets but perform less well with large heterogeneous training-sets because of edge effects, overfitting, secondary gradients and other sources of noise (Juggins and Birks, 2012; Juggins, 2013). The modern analogue technique, on the other hand, can perform well with large data-sets because it can model local relationships (Birks et al., 2010). However, it can produce ‘noisy’ reconstructions because it can model too much local structure in the training-set due to spatial autocorrelation (Telford and Birks, 2005), particularly when there are no analogues or only poor analogues. A small number of analogues will tend to produce “spiky” reconstructions, whereas a larger number will dampen out fine-scale variation and produce a “flatter” profile.

LW- WAPLS is a compromise between the “local” modelling aspect of the modern analogue technique and the “global” modelling aspect of WAPLS, as it seeks to exploit the best features of both approaches (Juggins and Birks, 2012). It is very much a “hybrid” method that takes advantage of the modern analogue technique and of WA/WAPLS. It first selects a local training-set of size *k* for a fossil sample using a distance (=dissimilarity) criterion or a predefined numerical criterion (Simpson, 2012) in the modern analogue technique. A much larger number of analogues (at least 20; Juggins and Birks, 2012) than in the conventional modern analogue method reduces the autocorrelation problem. Moreover, WAPLS, rather than averaging reconstructions derived from the modern analogue technique, is then applied to develop a reconstruction for each fossil sample based on the local training-set, which potentially reduces uncertainties. In other words, LW-WAPLS helps to minimize the problem of modern sample selection for traditional transfer-function methods (e.g. WA, WAPLS) and analogue failure (e.g. too few analogues) for the modern analogue technique. It exploits the advantage of increased environmental and biological coverage given by very large training-sets without suffering the disadvantage of increased prediction error (Juggins and Birks, 2012). Therefore, it is potentially a useful

**Table 3**
Error estimates (RMSEP) of mean annual temperature (MAT, °C), mean temperature of the warmest month (MTWM, °C), mean temperature of the coldest month (MTCM, °C) and mean annual precipitation (MAP, mm) for various reconstruction models. The training-sets were chosen on distance range or by the modern analogue approach.[a].

| Model | Parameter | Sample number | MAT | | MTWM | | MTCM | | MAP | |
|---|---|---|---|---|---|---|---|---|---|---|
| | | | *RMSEP* | $R^2$ | *RMSEP* | $R^2$ | *RMSEP* | $R^2$ | *RMSEP* | $R^2$ |
| BAM | 500 km | 769 | 3.968 | 0.648 | 3.669 | 0.742 | 3.635 | 0.544 | 112.648 | 0.725 |
| | 600 km | 1033 | 4.048 | 0.644 | 3.678 | 0.745 | 3.794 | 0.662 | 117.804 | 0.762 |
| | 700 km | 1539 | 4.070 | 0.624 | 3.713 | 0.758 | 3.683 | 0.758 | 124.717 | 0.881 |
| | 800 km | 1767 | 4.100 | 0.623 | 3.731 | 0.802 | 3.814 | 0.780 | 126.778 | 0.894 |
| | 900 km | 2012 | 4.158 | 0.621 | 3.760 | 0.833 | 3.890 | 0.805 | 128.371 | 0.890 |
| | 1000 km | 2111 | 4.236 | 0.619 | 3.786 | 0.858 | 3.863 | 0.821 | 130.413 | 0.885 |
| | 1100 km | 2350 | 4.369 | 0.612 | 3.783 | 0.878 | 3.965 | 0.820 | 135.510 | 0.886 |
| | 1200 km | 2454 | 4.382 | 0.587 | 3.809 | 0.804 | 4.046 | 0.819 | 144.119 | 0.877 |
| | 1300 km | 2649 | 4.384 | 0.582 | 3.810 | 0.829 | 4.107 | 0.830 | 153.402 | 0.886 |
| | 1400 km | 2866 | 4.411 | 0.535 | 3.814 | 0.855 | 4.232 | 0.838 | 158.452 | 0.888 |
| | 1500 km | 3052 | 4.480 | 0.534 | 3.826 | 0.852 | 4.409 | 0.842 | 165.973 | 0.888 |
| | 1600 km | 3609 | 4.633 | 0.516 | 3.838 | 0.877 | 4.620 | 0.845 | 170.605 | 0.891 |
| | 1700 km | 3876 | 4.637 | 0.507 | 3.848 | 0.894 | 4.934 | 0.847 | 186.381 | 0.889 |
| | 1800 km | 4056 | 4.641 | 0.494 | 3.898 | 0.811 | 5.099 | 0.850 | 188.885 | 0.894 |
| | 1900 km | 4110 | 4.677 | 0.494 | 3.968 | 0.828 | 5.087 | 0.853 | 188.165 | 0.894 |
| | 2000 km | 4226 | 4.700 | 0.470 | 3.978 | 0.845 | 5.090 | 0.854 | 189.824 | 0.897 |
| | All dataset | 4878 | 4.795 | 0.459 | 4.041 | 0.854 | 5.179 | 0.813 | 193.775 | 0.865 |
| WA classical | 500 km | 769 | 6.067 | 0.568 | 5.799 | 0.463 | 5.924 | 0.543 | 150.325 | 0.754 |
| | 600 km | 1033 | 6.107 | 0.551 | 5.840 | 0.453 | 6.033 | 0.540 | 155.610 | 0.754 |
| | 700 km | 1539 | 6.117 | 0.546 | 5.930 | 0.384 | 6.095 | 0.533 | 157.378 | 0.751 |
| | 800 km | 1767 | 6.127 | 0.546 | 5.946 | 0.380 | 6.235 | 0.533 | 176.948 | 0.705 |
| | 900 km | 2012 | 6.157 | 0.512 | 5.968 | 0.366 | 6.254 | 0.517 | 177.432 | 0.703 |
| | 1000 km | 2111 | 6.314 | 0.508 | 6.086 | 0.348 | 6.264 | 0.512 | 185.250 | 0.676 |
| | 1100 km | 2350 | 6.467 | 0.490 | 6.105 | 0.318 | 6.303 | 0.511 | 186.316 | 0.666 |
| | 1200 km | 2454 | 6.496 | 0.486 | 6.154 | 0.295 | 6.366 | 0.484 | 186.475 | 0.657 |
| | 1300 km | 2649 | 6.549 | 0.483 | 6.203 | 0.372 | 6.415 | 0.484 | 186.476 | 0.643 |
| | 1400 km | 2866 | 6.626 | 0.473 | 6.252 | 0.349 | 6.490 | 0.481 | 195.077 | 0.632 |
| | 1500 km | 3052 | 6.679 | 0.450 | 6.292 | 0.353 | 6.593 | 0.473 | 198.013 | 0.610 |
| | 1600 km | 3609 | 6.848 | 0.435 | 6.351 | 0.339 | 6.787 | 0.463 | 201.831 | 0.554 |
| | 1700 km | 3876 | 6.874 | 0.413 | 6.401 | 0.329 | 6.845 | 0.460 | 206.733 | 0.537 |
| | 1800 km | 4056 | 6.898 | 0.406 | 6.412 | 0.320 | 7.093 | 0.456 | 215.827 | 0.523 |
| | 1900 km | 4110 | 6.911 | 0.397 | 6.421 | 0.310 | 7.118 | 0.450 | 217.600 | 0.520 |
| | 2000 km | 4226 | 7.049 | 0.384 | 6.435 | 0.301 | 7.165 | 0.447 | 221.127 | 0.518 |
| | All dataset | 4878 | 7.052 | 0.382 | 6.439 | 0.278 | 7.252 | 0.432 | 222.251 | 0.495 |
| | 10-analogues | 421 | 5.744 | 0.603 | 5.301 | 0.626 | 5.286 | 0.683 | 139.679 | 0.735 |
| | 15-analogues | 516 | 5.778 | 0.592 | 5.351 | 0.739 | 5.297 | 0.639 | 149.608 | 0.724 |
| | 20-analogues | 597 | 5.908 | 0.579 | 5.473 | 0.764 | 5.327 | 0.633 | 161.899 | 0.696 |
| | 25-analogues | 634 | 6.017 | 0.599 | 5.596 | 0.683 | 5.334 | 0.682 | 165.307 | 0.685 |
| | 30-analogues | 728 | 6.021 | 0.583 | 5.717 | 0.631 | 5.629 | 0.664 | 176.974 | 0.599 |
| | 35-analogues | 845 | 6.071 | 0.590 | 5.839 | 0.660 | 5.702 | 0.690 | 186.635 | 0.702 |
| | 40-analogues | 893 | 6.093 | 0.585 | 5.861 | 0.693 | 5.757 | 0.666 | 188.236 | 0.674 |
| | 45-analogues | 916 | 6.120 | 0.600 | 5.883 | 0.627 | 5.839 | 0.680 | 197.638 | 0.732 |
| | 50-analogues | 934 | 6.270 | 0.577 | 5.956 | 0.656 | 5.878 | 0.589 | 207.784 | 0.544 |
| WA inverse | 500 km | 769 | 3.881 | 0.554 | 3.514 | 0.466 | 3.283 | 0.389 | 135.717 | 0.591 |
| | 600 km | 1033 | 3.697 | 0.459 | 3.528 | 0.495 | 3.353 | 0.495 | 144.947 | 0.633 |
| | 700 km | 1539 | 3.832 | 0.493 | 3.531 | 0.418 | 3.556 | 0.570 | 174.177 | 0.764 |
| | 800 km | 1767 | 3.943 | 0.443 | 3.589 | 0.459 | 3.784 | 0.599 | 181.690 | 0.779 |
| | 900 km | 2012 | 4.042 | 0.406 | 3.595 | 0.474 | 4.003 | 0.624 | 182.980 | 0.773 |
| | 1000 km | 2111 | 4.058 | 0.373 | 3.595 | 0.447 | 4.018 | 0.645 | 185.758 | 0.765 |
| | 1100 km | 2350 | 4.061 | 0.337 | 3.603 | 0.511 | 4.053 | 0.663 | 185.986 | 0.782 |
| | 1200 km | 2454 | 4.108 | 0.332 | 3.627 | 0.513 | 4.129 | 0.666 | 193.168 | 0.776 |
| | 1300 km | 2649 | 4.155 | 0.310 | 3.641 | 0.497 | 4.272 | 0.678 | 220.564 | 0.762 |
| | 1400 km | 2866 | 4.181 | 0.284 | 3.654 | 0.522 | 4.420 | 0.694 | 223.156 | 0.776 |
| | 1500 km | 3052 | 4.293 | 0.260 | 3.688 | 0.380 | 4.633 | 0.705 | 226.080 | 0.789 |
| | 1600 km | 3609 | 4.388 | 0.253 | 3.734 | 0.382 | 4.909 | 0.711 | 231.989 | 0.796 |
| | 1700 km | 3876 | 4.486 | 0.214 | 3.747 | 0.402 | 5.083 | 0.739 | 239.529 | 0.814 |
| | 1800 km | 4056 | 4.523 | 0.201 | 3.790 | 0.391 | 5.197 | 0.753 | 240.702 | 0.825 |
| | 1900 km | 4110 | 4.540 | 0.203 | 3.800 | 0.388 | 5.245 | 0.752 | 241.466 | 0.824 |
| | 2000 km | 4226 | 4.552 | 0.204 | 3.817 | 0.381 | 5.256 | 0.753 | 242.485 | 0.826 |
| | All dataset | 4878 | 4.752 | 0.200 | 3.924 | 0.392 | 5.507 | 0.816 | 263.099 | 0.859 |
| | 10-analogues | 421 | 4.052 | 0.679 | 3.702 | 0.609 | 3.646 | 0.735 | 131.263 | 0.831 |
| | 15-analogues | 516 | 4.059 | 0.658 | 3.709 | 0.684 | 3.786 | 0.754 | 131.904 | 0.787 |
| | 20-analogues | 597 | 4.061 | 0.624 | 3.717 | 0.71 | 3.925 | 0.774 | 148.253 | 0.702 |
| | 25-analogues | 634 | 4.111 | 0.652 | 3.752 | 0.624 | 4.064 | 0.793 | 155.351 | 0.845 |
| | 30-analogues | 728 | 4.111 | 0.632 | 3.844 | 0.66 | 4.203 | 0.812 | 182.747 | 0.626 |
| | 35-analogues | 845 | 4.118 | 0.646 | 3.848 | 0.658 | 4.342 | 0.831 | 183.053 | 0.644 |
| | 40-analogues | 893 | 4.120 | 0.628 | 3.852 | 0.657 | 4.481 | 0.851 | 195.001 | 0.611 |
| | 45-analogues | 916 | 4.140 | 0.675 | 3.855 | 0.657 | 4.620 | 0.870 | 203.337 | 0.666 |
| | 50-analogues | 934 | 4.151 | 0.594 | 3.855 | 0.656 | 4.759 | 0.889 | 230.600 | 0.646 |
| WA non-linear | 500 km | 769 | 3.314 | 0.681 | 3.144 | 0.710 | 3.293 | 0.425 | 131.273 | 0.617 |
| | 600 km | 1033 | 3.564 | 0.590 | 3.169 | 0.674 | 3.471 | 0.548 | 141.805 | 0.648 |

(*continued on next page*)

**Table 3** (*continued*)

| Model | Parameter | Sample number | MAT | | MTWM | | MTCM | | MAP | |
|---|---|---|---|---|---|---|---|---|---|---|
| | | | *RMSEP* | $R^2$ | *RMSEP* | $R^2$ | *RMSEP* | $R^2$ | *RMSEP* | $R^2$ |
| | 700 km | 1539 | 3.758 | 0.647 | 3.202 | 0.653 | 3.504 | 0.582 | 164.616 | 0.790 |
| | 800 km | 1767 | 3.919 | 0.603 | 3.304 | 0.628 | 3.718 | 0.613 | 173.051 | 0.799 |
| | 900 km | 2012 | 4.042 | 0.571 | 3.356 | 0.523 | 3.910 | 0.641 | 176.295 | 0.790 |
| | 1000 km | 2111 | 4.057 | 0.540 | 3.402 | 0.527 | 3.906 | 0.665 | 179.216 | 0.781 |
| | 1100 km | 2350 | 4.086 | 0.512 | 3.214 | 0.519 | 3.957 | 0.679 | 180.264 | 0.796 |
| | 1200 km | 2454 | 4.122 | 0.506 | 3.279 | 0.512 | 4.036 | 0.681 | 187.379 | 0.789 |
| | 1300 km | 2649 | 4.194 | 0.493 | 3.366 | 0.511 | 4.184 | 0.691 | 212.572 | 0.779 |
| | 1400 km | 2866 | 4.223 | 0.468 | 3.622 | 0.482 | 4.326 | 0.707 | 214.474 | 0.793 |
| | 1500 km | 3052 | 4.270 | 0.436 | 3.985 | 0.461 | 4.478 | 0.724 | 213.454 | 0.812 |
| | 1600 km | 3609 | 4.389 | 0.435 | 3.986 | 0.461 | 4.777 | 0.726 | 217.944 | 0.820 |
| | 1700 km | 3876 | 4.489 | 0.400 | 3.991 | 0.460 | 4.903 | 0.757 | 221.480 | 0.841 |
| | 1800 km | 4056 | 4.519 | 0.388 | 4.012 | 0.460 | 5.017 | 0.770 | 222.503 | 0.850 |
| | 1900 km | 4110 | 4.535 | 0.389 | 4.030 | 0.459 | 5.063 | 0.769 | 222.823 | 0.850 |
| | 2000 km | 4226 | 4.547 | 0.391 | 4.041 | 0.459 | 5.073 | 0.770 | 224.316 | 0.851 |
| | All dataset | 4878 | 4.612 | 0.321 | 4.045 | 0.459 | 5.287 | 0.827 | 235.678 | 0.785 |
| | 10-analogues | 421 | 3.876 | 0.652 | 3.561 | 0.735 | 3.912 | 0.745 | 151.872 | 0.676 |
| | 15-analogues | 516 | 3.932 | 0.678 | 3.594 | 0.773 | 3.736 | 0.763 | 152.764 | 0.599 |
| | 20-analogues | 597 | 3.954 | 0.798 | 3.655 | 0.839 | 3.661 | 0.781 | 158.724 | 0.551 |
| | 25-analogues | 634 | 3.955 | 0.704 | 3.691 | 0.679 | 3.786 | 0.800 | 171.404 | 0.592 |
| | 30-analogues | 728 | 3.980 | 0.727 | 3.801 | 0.680 | 3.911 | 0.818 | 173.696 | 0.662 |
| | 35-analogues | 845 | 4.008 | 0.685 | 3.802 | 0.697 | 4.036 | 0.836 | 177.068 | 0.595 |
| | 40-analogues | 893 | 4.074 | 0.789 | 3.809 | 0.711 | 4.160 | 0.854 | 183.219 | 0.694 |
| | 45-analogues | 916 | 4.079 | 0.766 | 3.812 | 0.727 | 4.285 | 0.873 | 186.486 | 0.613 |
| | 50-analogues | 934 | 4.095 | 0.752 | 3.836 | 0.749 | 4.410 | 0.891 | 191.087 | 0.552 |
| WAPLS Component2 | 500 km | 769 | 3.532 | 0.630 | 3.236 | 0.694 | 3.245 | 0.405 | 131.767 | 0.615 |
| | 600 km | 1033 | 3.793 | 0.595 | 3.255 | 0.686 | 3.337 | 0.529 | 137.902 | 0.668 |
| | 700 km | 1539 | 3.823 | 0.597 | 3.307 | 0.681 | 3.356 | 0.617 | 166.825 | 0.784 |
| | 800 km | 1767 | 4.005 | 0.579 | 3.432 | 0.679 | 3.559 | 0.645 | 174.414 | 0.796 |
| | 900 km | 2012 | 4.105 | 0.530 | 3.503 | 0.656 | 3.692 | 0.680 | 176.015 | 0.790 |
| | 1000 km | 2111 | 4.103 | 0.535 | 3.508 | 0.631 | 3.689 | 0.701 | 177.190 | 0.786 |
| | 1100 km | 2350 | 4.107 | 0.513 | 3.521 | 0.626 | 3.756 | 0.711 | 180.084 | 0.796 |
| | 1200 km | 2454 | 4.187 | 0.515 | 3.612 | 0.621 | 3.882 | 0.705 | 188.001 | 0.788 |
| | 1300 km | 2649 | 4.247 | 0.528 | 3.727 | 0.620 | 4.054 | 0.710 | 219.312 | 0.765 |
| | 1400 km | 2866 | 4.329 | 0.507 | 3.805 | 0.619 | 4.278 | 0.713 | 225.505 | 0.772 |
| | 1500 km | 3052 | 4.430 | 0.509 | 3.850 | 0.617 | 4.506 | 0.721 | 230.620 | 0.780 |
| | 1600 km | 3609 | 4.533 | 0.499 | 3.957 | 0.601 | 4.825 | 0.721 | 239.537 | 0.783 |
| | 1700 km | 3876 | 4.668 | 0.451 | 4.055 | 0.599 | 5.045 | 0.743 | 250.982 | 0.796 |
| | 1800 km | 4056 | 4.699 | 0.431 | 4.164 | 0.584 | 5.184 | 0.755 | 253.112 | 0.806 |
| | 1900 km | 4110 | 4.726 | 0.435 | 4.183 | 0.576 | 5.244 | 0.752 | 254.433 | 0.804 |
| | 2000 km | 4226 | 4.725 | 0.435 | 4.195 | 0.572 | 5.253 | 0.753 | 255.403 | 0.807 |
| | All dataset | 4878 | 5.446 | 0.277 | 3.947 | 0.590 | 5.459 | 0.815 | 373.844 | 0.850 |
| | 10-analogues | 421 | 3.813 | 0.796 | 3.493 | 0.755 | 3.609 | 0.731 | 126.040 | 0.785 |
| | 15-analogues | 516 | 3.832 | 0.748 | 3.513 | 0.802 | 3.759 | 0.747 | 128.912 | 0.644 |
| | 20-analogues | 597 | 3.894 | 0.681 | 3.521 | 0.826 | 3.409 | 0.763 | 130.917 | 0.679 |
| | 25-analogues | 634 | 3.894 | 0.654 | 3.575 | 0.835 | 4.059 | 0.779 | 165.769 | 0.696 |
| | 30-analogues | 728 | 3.923 | 0.724 | 3.688 | 0.827 | 4.210 | 0.796 | 168.710 | 0.719 |
| | 35-analogues | 845 | 3.975 | 0.691 | 3.702 | 0.773 | 4.360 | 0.812 | 175.867 | 0.552 |
| | 40-analogues | 893 | 3.986 | 0.770 | 3.815 | 0.745 | 4.510 | 0.828 | 189.667 | 0.510 |
| | 45-analogues | 916 | 3.989 | 0.687 | 3.822 | 0.675 | 4.660 | 0.844 | 257.028 | 0.710 |
| | 50-analogues | 934 | 4.000 | 0.718 | 3.713 | 0.662 | 4.811 | 0.860 | 276.962 | 0.544 |
| LW-WA | k = 10 | – | 3.476 | 0.548 | 3.416 | 0.721 | 3.784 | 0.589 | 149.081 | 0.576 |
| | k = 15 | – | 3.421 | 0.539 | 3.437 | 0.726 | 3.767 | 0.695 | 148.693 | 0.763 |
| | k = 20 | – | 3.420 | 0.709 | 3.442 | 0.73 | 3.511 | 0.770 | 142.530 | 0.797 |
| | k = 25 | – | 3.436 | 0.688 | 3.545 | 0.749 | 3.890 | 0.799 | 143.323 | 0.761 |
| | k = 30 | – | 3.581 | 0.670 | 3.675 | 0.804 | 4.069 | 0.824 | 143.762 | 0.757 |
| | k = 35 | – | 3.638 | 0.662 | 3.694 | 0.775 | 4.001 | 0.845 | 172.995 | 0.740 |
| | k = 40 | – | 3.790 | 0.631 | 3.733 | 0.745 | 3.979 | 0.863 | 178.126 | 0.717 |
| | k = 45 | – | 3.793 | 0.616 | 3.755 | 0.724 | 4.059 | 0.866 | 193.094 | 0.698 |
| | k = 50 | – | 3.888 | 0.556 | 3.755 | 0.712 | 4.190 | 0.878 | 196.211 | 0.662 |
| LW-WAPLS | k = 10 | – | 3.347 | 0.652 | 3.062 | 0.810 | 3.507 | 0.794 | 158.050 | 0.678 |
| | k = 15 | – | 3.398 | 0.619 | 3.060 | 0.804 | 3.518 | 0.805 | 162.539 | 0.758 |
| | k = 20 | – | 3.428 | 0.596 | 3.055 | 0.785 | 3.323 | 0.811 | 169.625 | 0.844 |
| | k = 25 | – | 4.348 | 0.691 | 3.141 | 0.728 | 3.613 | 0.839 | 157.245 | 0.838 |
| | k = 30 | – | 4.084 | 0.682 | 3.149 | 0.826 | 3.988 | 0.853 | 157.004 | 0.833 |
| | k = 35 | – | 4.191 | 0.647 | 3.157 | 0.822 | 4.051 | 0.852 | 158.595 | 0.814 |
| | k = 40 | – | 4.248 | 0.614 | 3.170 | 0.783 | 4.056 | 0.853 | 158.060 | 0.760 |
| | k = 45 | – | 4.346 | 0.589 | 3.181 | 0.726 | 4.305 | 0.874 | 160.769 | 0.759 |
| | k = 50 | – | 4.411 | 0.532 | 3.204 | 0.816 | 4.429 | 0.886 | 160.385 | 0.753 |

[a] BAM: best analogue method; WA = weighted averaging; non-linear = non-linear monotonic deshrinking; PLS = partial least squares; LW = locally-weighted.

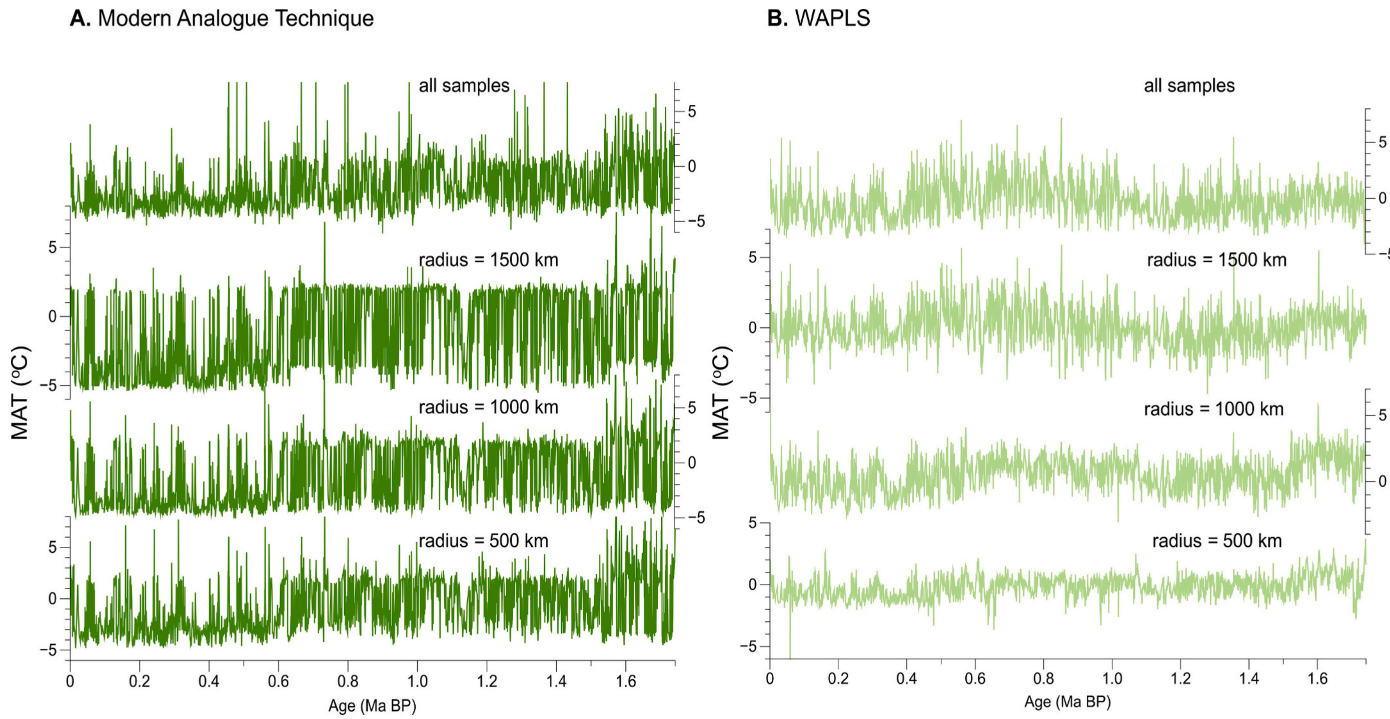


**Fig. 6.** Temperature reconstructions for Zoige Basin core ZB13-C2 using A. the best analogue method (BAM) and B. weighted-average partial least squares (WAPLS). Results are shown for various modern training-sets using different distances for sample inclusion and for all samples.

approach that can minimize the uncertainties for climate reconstructions at the broad glacial-interglacial scale (Birks, 2012; Juggins and Birks, 2012). The WAPLS part could be replaced with other regression and calibration methods such as two-way WA (Hubener et al., 2008; Lu et al., 2011; Juggins and Birks, 2012), non-linear WA (Marchetto, 1994; Birks and Simpson, 2013), or Gaussian logit regression and maximum-likelihood calibration (Hubener et al., 2008).

LW-WAPLS was used for the final quantitative climate reconstruction in our study. First, based on the modern data-set, a "local" or dynamic (Birks, 1998) training-set of analogues in the modern data-set was generated for each of the 2787 fossil samples using the modern analogue technique and squared-chord distance (Simpson, 2012). The results of leave-one-out cross-validation show that the RMSEP value when selecting 10–20 modern analogues is lower than with 21–50 analogues (Tables 2 and 3), while the climatic gradient represented does not decrease. If $k < 20$ analogues are selected, it is not statistically appropriate for the following WAPLS step. Moreover, the analogue quality and spatial distribution of the modern analogues for $k = 20$ appear to be representative (Fig. S4). Therefore, 20 modern analogues for each fossil sample are in this case considered to be an appropriate choice. In total, 597 analogue samples comprise the training-set for all 2787 fossil pollen samples in core ZB13-C2 (Fig. 3A). Second, based on the "local" analogue training-set for each sample, WAPLS (Ter Braak and Juggins, 1993) was used to reconstruct the down-core climate variables. We also reconstructed the down-core climate variables using 30, 40, and 50 modern analogues as a comparison with reconstructions based on 20 analogues (see Figs. S4 and S5).

In addition to LW-WAPLS, we also performed BAM, two-way WA (Birks et al., 1990a), and WAPLS (Ter Braak and Juggins, 1993) with the modern pollen–climate training-set and fossil pollen data for comparison (Table 2). Model error estimates of the different models are all based on leave-one-out cross-validation.

### 2.6. Model evaluation and validation

The similarity between the modern training-set and the fossil pollen assemblages was evaluated based on the minimum dissimilarity between each fossil sample and each best analogue from training-set samples, using squared chord distance (SCD) (Simpson, 2012). The distances smaller than the 5th percentile of all distances between the training-set samples can be considered to be "good analogues", while samples with distances larger than the 10th percentile can be regarded as "no-analogue" assemblages (Simpson, 2012).

As a measure of model performance, the root mean square error of prediction (RMSEP) incorporates both random and systematic components of error. The random bootstrap sample-specific estimates of the standard error (Birks et al., 1990a) for each reconstructed value at the Zoige site were estimated as follows. All modern samples selected in LW-WAPLS were used to create a modern training-set consisting only of those modern samples selected for the LW-WAPLS. As LW-WAPLS does not yet have its own bootstrap evaluation function, this trimmed training-set was then used in a conventional WAPLS (Ter Braak and Juggins, 1993) with the Zoige fossil data to obtain bootstrap sample-specific estimates of uncertainties for each reconstructed value (Birks et al., 1990a). This application may overestimate the error as i) LW-WAPLS uses a local training-set for each sample and ii) LW-WAPLS has a good fitting ability for broad-scale climate change (Juggins and Birks, 2012). The systematic components of error represent the difference between the model predictions and the observed values and are calculated as the RMSEP for the training-set samples (Birks et al., 1990a).

Significance tests were used to assess the overall performance of the reconstructions for the entire core in addition to sample-specific error evaluation (Telford and Birks, 2011). A number of random reconstructions (999 in our case) were derived from the training-set. The proportion of variance explained by these random reconstructions was estimated using redundancy analysis (RDA), a linear-based constrained ordination technique (Ter Braak, 1994).

In order to evaluate the reconstruction results ecologically, weighted-average optima and tolerances of the major pollen taxa for the main climate variables in the calibration-set were estimated to detect the distributional and abundance characteristics of the different taxa along the environmental gradients. The Huisman-Olff-Fresco (HOF) model (Huisman et al., 1993; Jansen and Oksanen, 2013) was also used to investigate and model the relationships between the pollen percentages of the major taxa and contemporary climate variables based on the local training-set.

### 2.7. Other numerical analyses

Generalized additive models, a non-parametric extension of generalized linear models (Yee and Mitchell, 1991; Birks, 2012), were used to filter high frequency variability and extract the main trend within the reconstructed temperatures. Like LOESS, GAMs estimate smooth and non-linear trends in time-series and can handle the irregular spacing of samples in time; yet GAMs do not suffer from the subjectivity that plagues LOESS as a method for formal statistical inference (Simpson, 2018). The analysis of the Zoige temperature time-series using GAMs follows the main steps described by Simpson (2018). The Derive function was used to obtain the first derivative of the temperature trend and to identify intervals with major changes within these time-series.

### 2.8. Computing

All the numerical analyses were implemented in R version 3.4.0. (R Core Team, 2019) using functions in the following packages:

MRT: package "mvpart" (Therneau and Beth Atkinson, 2014)
H-cluster: package "stats" (R Core Team, 2019)
HOF: package "eHOF" (Jansen and Oksanen, 2013)
CCA, RDA, PCA: package "vegan" (Oksanen et al., 2019)
Timetrack: package "Analogue" (Simpson and Oksanen, 2020)
LWWA, MAT , WA , WAPLS: package "rioja" (Juggins, 2017)
LWWA, LW-WAPLS: package "Analogue" and "rioja" (Simpson and Oksanen, 2020; Juggins, 2017)
Significance test: package "palaeoSig" (Telford, 2019)
GAM: package "mgcv" (Wood, 2017)
Derive: package "numDeriv" (Gilbert and Varadhan, 2019)

## 3. Results and discussion

### 3.1. Advantages and limitations of the LW-WAPLS approach

The LW-WAPLS model for the Zoige site basically has lower RMSEP values than the modern analogue technique and traditional weighted-average transfer functions (Table 2). When 20 analogues for LW-WAPLS is selected, the RMSEP is 3.06 °C for MAT and 3.43 °C for MTWM (Table 1), which is almost less than that of the BAM ($k = 6$) and transfer functions, no matter what training-set range is used for them. For example, the MAT error of WAPLS (distance = 1500 km) is 3.85 °C, ~0.8 °C (21% larger) than that of LW-WAPLS when using $k = 20$. The lower RMSEP suggests LW-WAPLS is potentially a more robust model with our data.

The results of various models for pollen-inferred climate variables with plots of predicted (bootstrapping) against observed values are shown in Figs. S6–S8. The correlation of modern meteorological data with those predicted by the pollen-climate calibration-sets in statistical bootstrapping cross-validation illustrate the inference power of the models. In general, the temperature predictive power in BAM and WAPLS performed less well than in LW-WAPLS. None of the models for MAP performed well.

Modern analogue technique-based reconstructed temperatures of core ZB13-C2 show many spiky or flat changes (Fig. 6; Fig. S9).

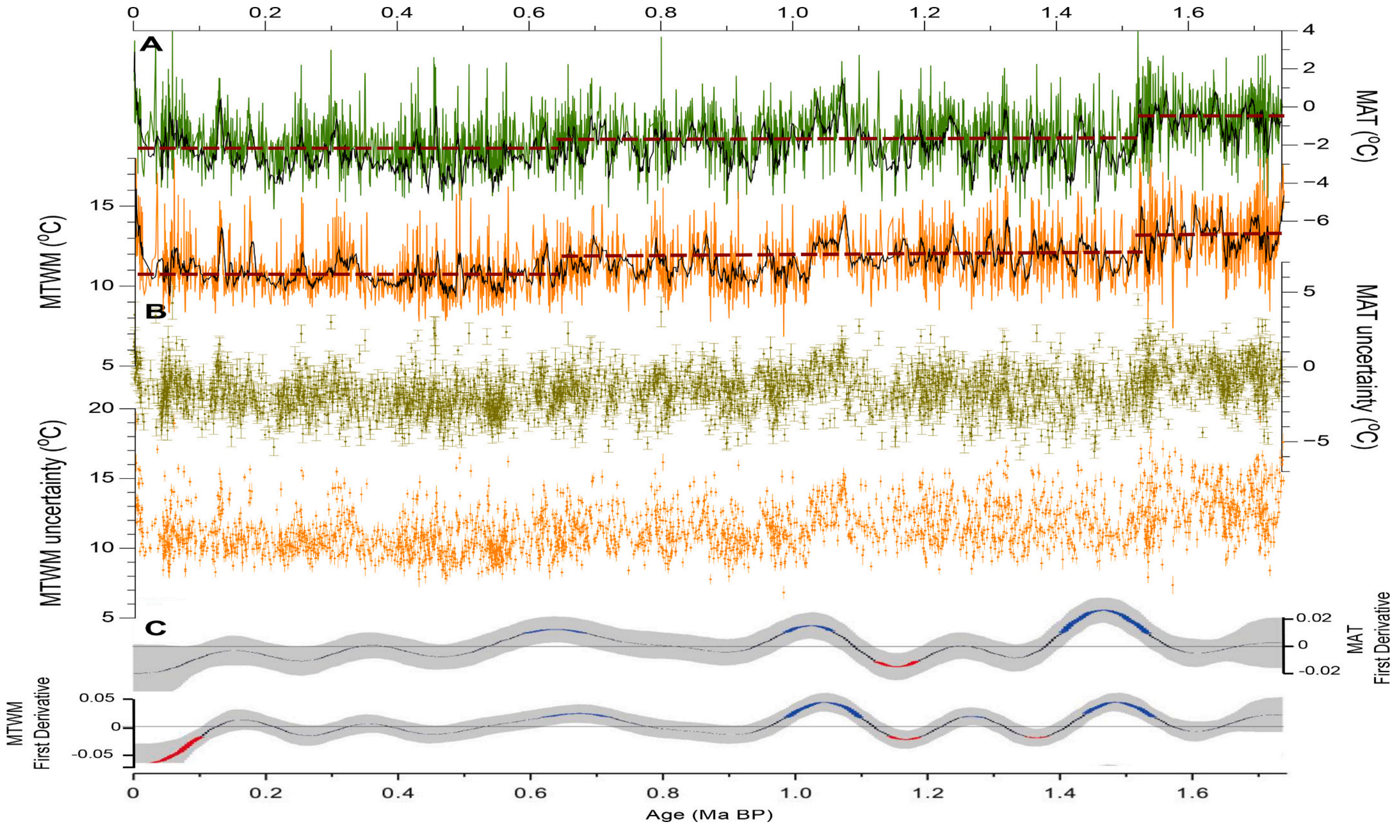


**Fig. 7.** Locally-weighted weighted-average partial least squares (LW-WAPLS)-based temperature reconstructions and associated bootstrap uncertainty estimates for Zoige Basin core ZB13-C2. A. Reconstructed mean annual temperature (MAT) and mean temperature of the warmest month (MTWM). Nine-point running means are shown as black lines. The dotted lines indicate the mean values for three major intervals. B. Bootstrap sample-specific estimates of uncertainties for each reconstructed temperature value. C. Estimated first derivatives (black lines) and 95% simultaneous confidence intervals (shaded grey bands) of the generalized additive model (GAM) trends fitted to the MAT and MTWM time-series. Blue/red colour indicates an interval with a major increase/decrease of MAT/MTWM. The GAMs detect significant temporal change at ~1.54 and 0.62 Ma BP. (For interpretation of the references to colour in this figure legend, the reader is referred to the web version of this article.)

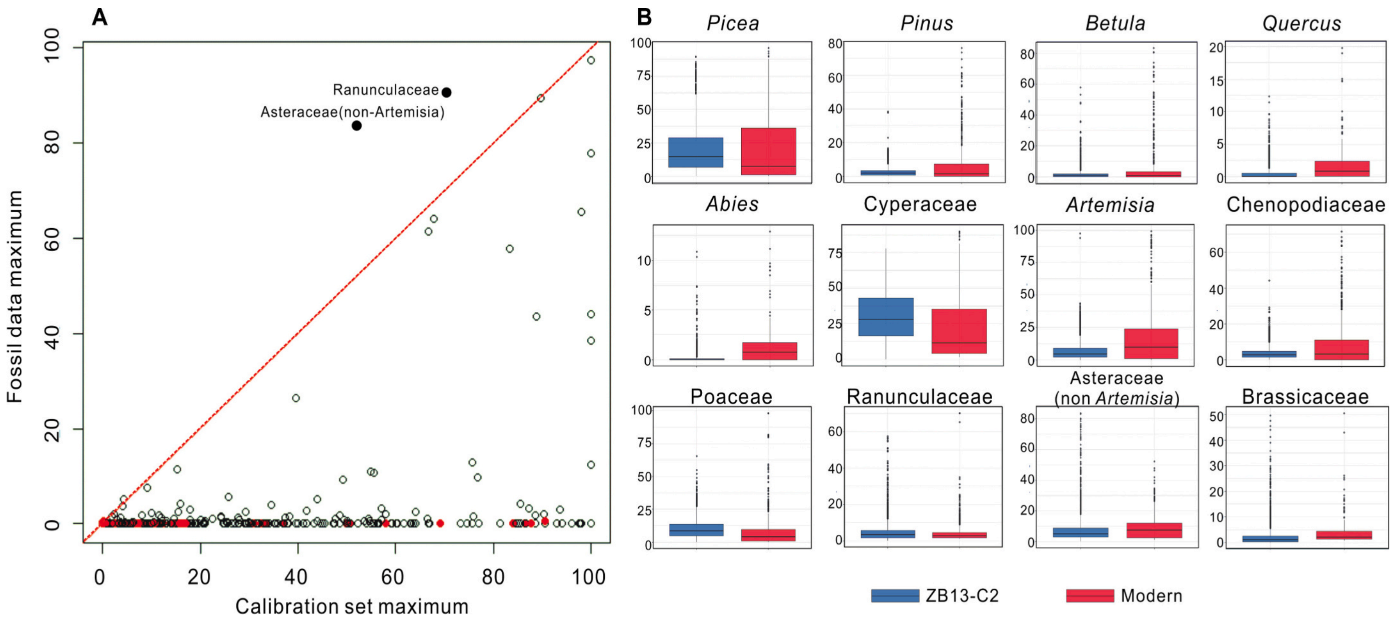


**Fig. 8.** The taxon coverage in the 597 modern pollen samples and 2787 fossil samples from Zoige Basin core ZB13-C2. A. Scatter plot of the maximum abundance of each taxon in the modern pollen data-set against that in the fossil pollen assemblages. The red circles indicate taxa in the modern pollen data-set that are not found in the fossil samples. B. Box-plots of median values and ranges of the percentages of the major pollen taxa (blue box: fossil samples, red box: modern samples). (For interpretation of the references to colour in this figure legend, the reader is referred to the web version of this article.)

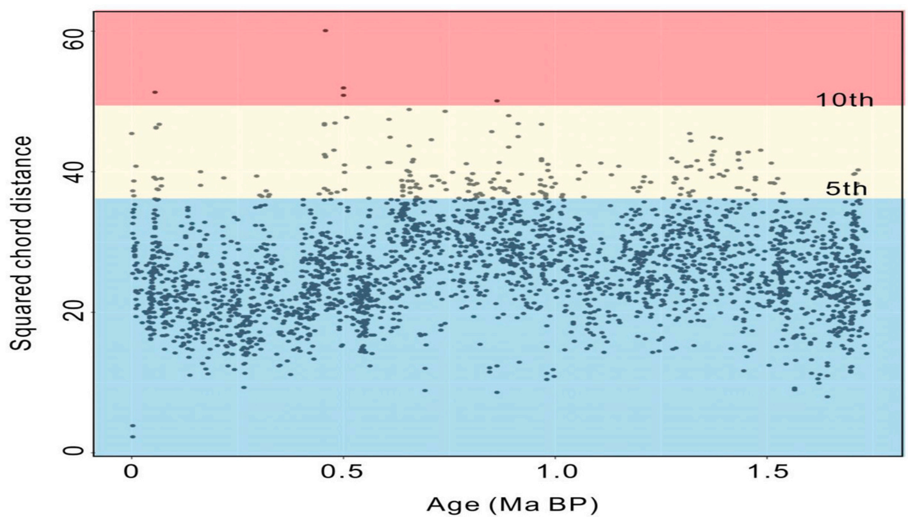


**Fig. 9.** Analogue quality for the reconstruction of mean temperature of the warmest month (MTWM) based on a goodness-of-fit analysis. The blue and cream shadings show the 5th and 10th percentiles of the pair-wise distribution of squared-chord distances between the fossil samples and the best analogues from the modern training-set, respectively. Distances smaller than the 5th percentile of all distances between the training-set samples are considered to be good "analogues", while distances larger than the 10th percentile are considered to be "no-analogue" assemblages. The results indicate a good match between fossil samples from the ZB13-C2 core and the modern pollen samples in the training-set. (For interpretation of the references to colour in this figure legend, the reader is referred to the web version of this article.)

Truncation problems occur when the training-set samples are chosen within a distance of 500, 1000, and 1500 km, but many spiky values are present and the uncertainty is much larger (Table 2) when the training-set samples are chosen with a distance of >1500 km. This could be associated with too few or too many analogues. The application of the modern analogue technique to core ZB13-C2 highlights the "spiky" and "flat" reconstruction problems (Fig. 6).

The WAPLS-based reconstructed temperature variability is very small when the training-set size is small (in the range 500–1000 km from the coring site), for example the glacial-interglacial MAT range is only 2 °C in most cases (Fig. 6). This magnitude is similar to that of tropical SST variabilities (Herbert et al., 2010) and the Holocene temperature range in the Zoige region (Liang et al., 2020), implying that these results may not be reliable. If the training-set is larger (e.g. distance = 1500 km), the RMSEP for MTWM is 3.85 °C, 21% larger than that of LW-WAPLS ($k = 20$) (Table 2). When all the modern pollen sites are included, the error is even larger. Cao et al. (2017) show that with respect to fossil spectra from the Tibetan Plateau and northern China, the spatial extent of modern calibration-sets should be restricted to radii between ca. 1000 and 1500 km because fine-scale calibration-sets (<800 km radius) will likely fail to include enough spatial variation in the modern pollen assemblages to reflect the temporal range shifts, while too broad a scale calibration-set (>1500 km radius) will include taxa with very different pollen–climate relationships resulting in increased model errors. Moreover, for the reconstructions with a calibration-set of >1500 km radius, the variability for the interval of ~1.74–1.03 Ma BP is relatively flat, like the results using the data-set within a distance of 1000 km (Fig. 6).

Furthermore, the results based on the BAM and WAPLS approaches are implausible ecologically for some intervals. For example, for 1.74–1.54 Ma BP, which has the highest deciduous tree abundances during the interglacials and warmer summer adapted *Artemisia* during the glacials, the WAPLS-based reconstructed interglacial temperature is lower than that of 1.03–0.62 Ma BP which includes quasi-absent *Quercus* and *Betula*, while the BAM-based glacial temperature for this interval has a similar low value to other intervals that include much less *Artemisia*.

In summary, the LW-WAPLS-based temperature reconstruction for the Zoige core is more reasonable compared with the BAM and WAPLS reconstructions in terms of i) smaller RMSEP error of the model; ii) much less spiky or truncated values (Fig. 7); iii) a MAT range from −4–2 °C, whose magnitude is roughly consistent with LGM–mid-Holocene temperature differences on the Tibetan Plateau inferred from various proxies (e.g. Thompson et al., 1989; Herzschuh et al., 2006) as discussed below; and iv) is more ecologically plausible.

Our application of LW-WAPLS to the ZB13-C2 long-term pollen sequence attests to the potential advantage of this method by combining the "local" modelling of the modern analogue technique and the "global" modelling of WAPLS and exploiting the strong features of both approaches (Juggins and Birks, 2012). However, the choice of the number of samples in the local training-set should be made very carefully as shown in the Zoige reconstruction procedure. As LW-WAPLS usually uses a large heterogeneous data-set, it may not perform well for a fine-scale climate change, as revealed by the Holocene temperature reconstruction in the Zoige region (Liang et al., 2020).

Another limitation of LW-WAPLS in this Zoige reconstruction, like with other statistical models, is that the effects of different atmospheric $CO_2$ concentrations for glacials and interglacials on plant distribution (Wu et al., 2007a, 2007b; Herzschuh et al., 2011) are not assessed or taken into account. In glacial times, low atmospheric $CO_2$ concentrations globally promoted the expansion of drought-resistant vegetation (Polley et al., 1993; Prentice and Harrison, 2009). Izumi and Bartlein (2016) used an inverse modelling procedure to reconstruct LGM climates from North American fossil pollen data. They found that although lower atmospheric $CO_2$ concentrations influence pollen-based LGM moisture reconstructions, they do not significantly affect temperature reconstructions over most of North America. In any case, the lower $CO_2$ concentrations during the glacials may cause some uncertainties; quantifying this effect requires more research in the future (Chevalier et al., 2020b).

### *3.2. Temperature variabilities over the past 1.74 Ma*

The pollen-derived mean annual and warmest month temperature (MAT and MTWM) reconstructions using LW-WAPLS show a general stepwise cooling trend from 1.74 to 1.54, 1.54 to 0.62, and 0.62 to 0 Ma BP (Fig. 7). The most obvious cooling occurs at 1.54 Ma BP. The generalized additive model first derivative further reveals that the biggest changes in temperature occurred around 1.54 and 0.62 Ma BP (Fig. 7). MTCM reconstruction (Fig. S11) is not used here due to its potentially large uncertainties from both the climatic and ecological views as discussed below.

MAT and MTWM show regular variability ranging from −4 to 2 °C and from 8 to 16 °C, respectively. The maximum interglacial MAT/MTWM is 4.5/20.31 °C, while the minimum glacial MAT/MTWM is −5.79/6.83 °C. They suggest mostly ~4–5 °C (MAT) and 5–6 °C (MTWM) glacial-interglacial variabilities for the last 1.74 Ma. During the interval from 0.62 Ma BP onwards, temperature during both glacials and interglacials shows the lowest values, with no large ranges after ~0.42 Ma BP, a feature also revealed by ice cores (Petit et al., 1999;

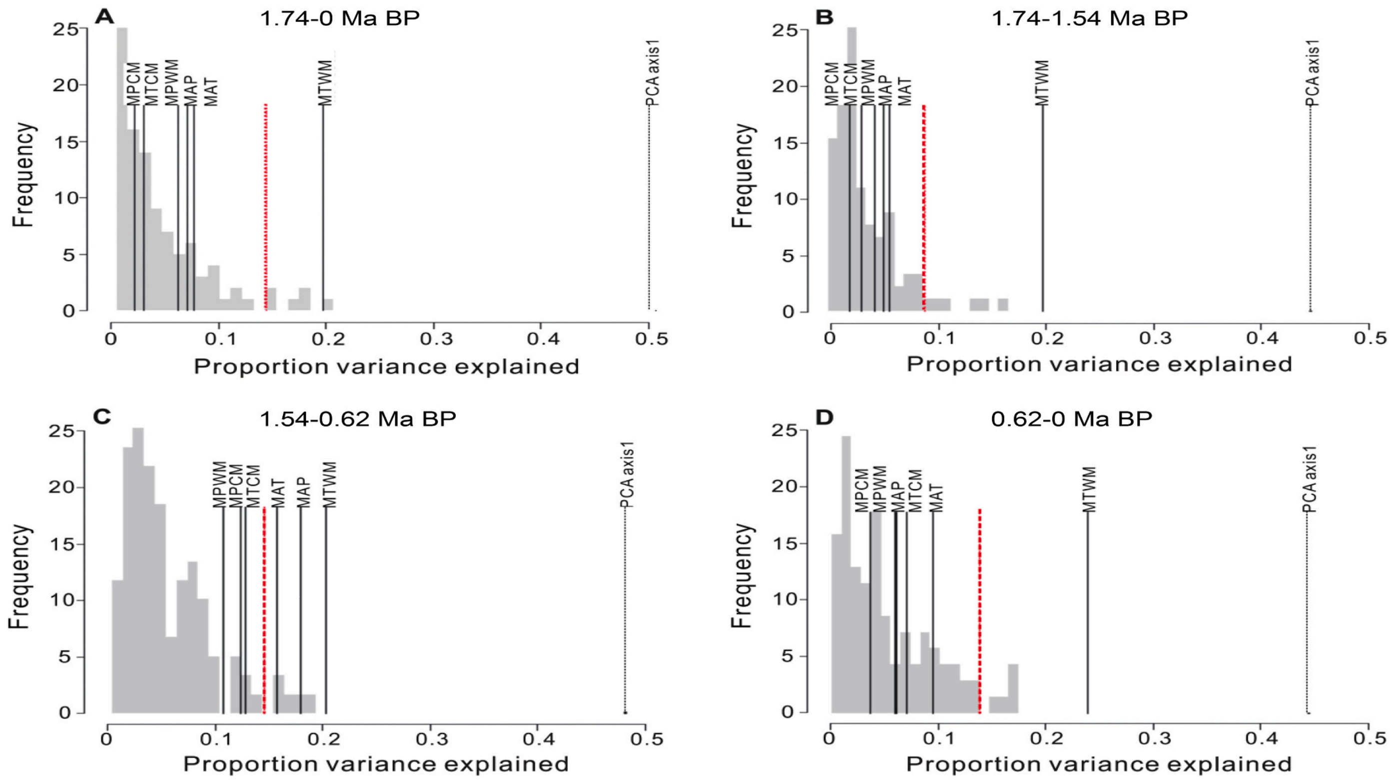


**Fig. 10.** Significance test results of the pollen-based climate reconstructions for the Zoige Basin core ZB13-C2. The red line represents the test line of 95% significance level. The histogram in grey indicates the proportion of variance. The grey dotted line indicates the proportion of the variance explained by the first axis of a principal components analysis (PCA) of the fossil data. A. 1.74–0 Ma BP. B. 1.74–1.54 Ma BP. C. 1.54–0.62 Ma BP. D. 0.62–0 Ma BP. Variable abbreviations are explained in the caption for Fig. 4. (For interpretation of the references to colour in this figure legend, the reader is referred to the web version of this article.)

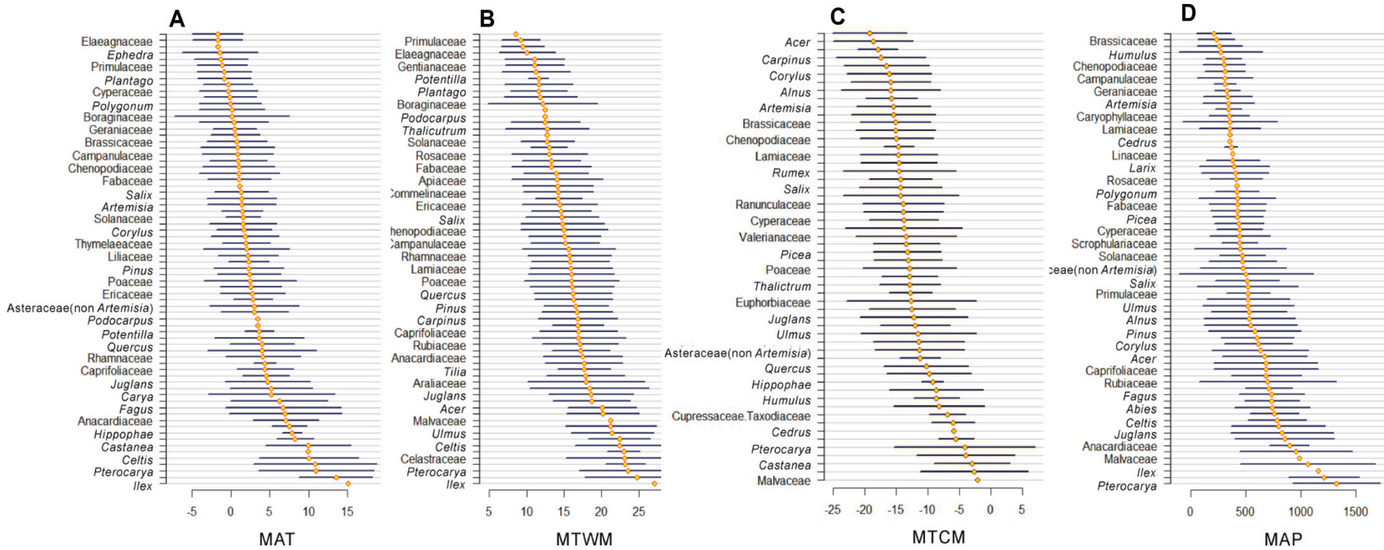


**Fig. 11.** Optima and tolerances of mean annual temperature (MAT), mean temperature of the warmest month (MTWM), mean temperature of the coldest month (MTCM), and mean annual precipitation (MAP) for selected pollen taxa based on weighted averaging (WA) regression. The modern pollen data are from the LW-WAPLS training-set. The yellow lines indicate the mean WA climate optima of the pollen taxa; the black lines indicate their WA tolerances. (For interpretation of the references to colour in this figure legend, the reader is referred to the web version of this article.)

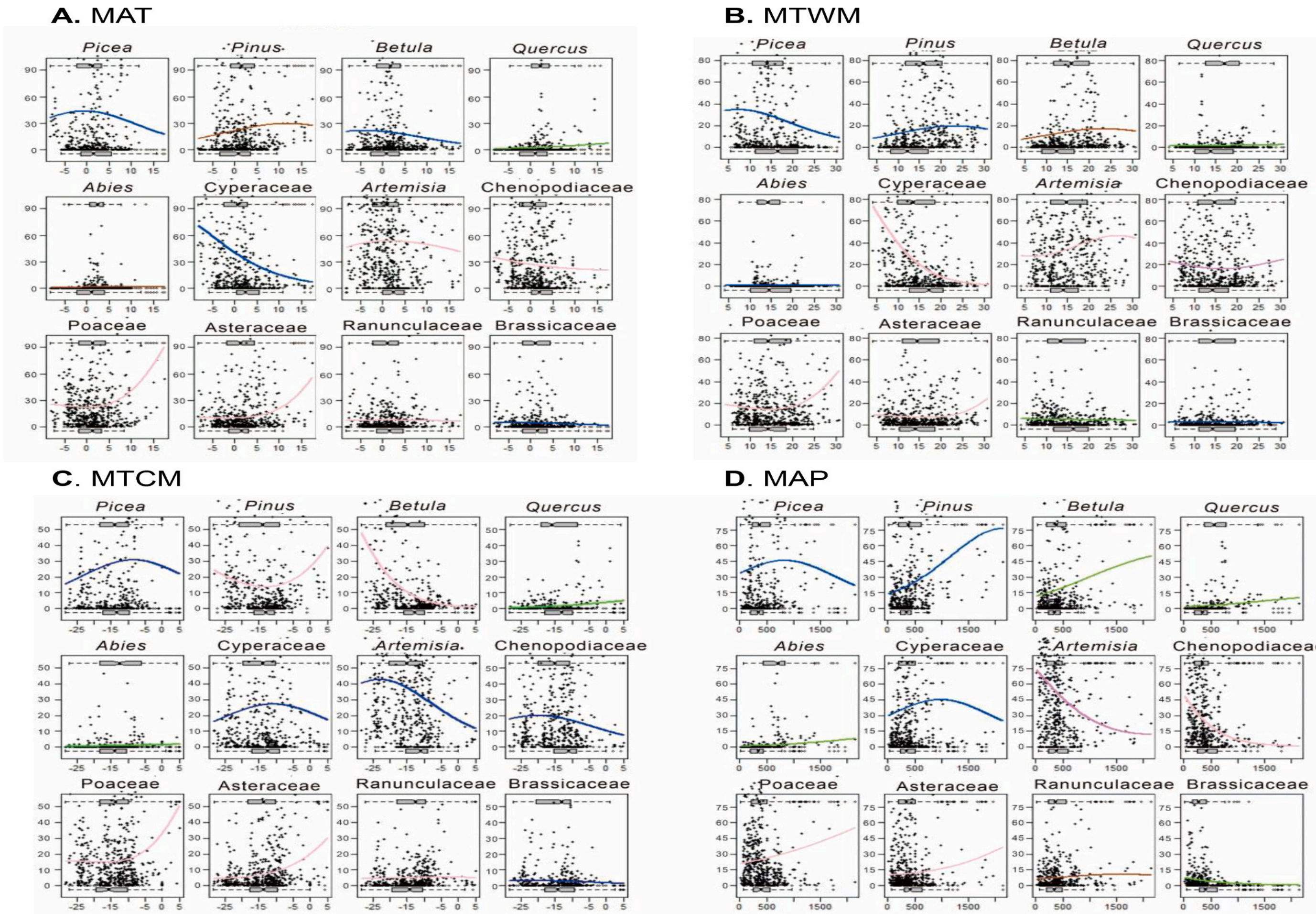


**Fig. 12.** Modelled relationships between percentages of selected modern pollen taxa and four climate variables – mean annual temperature (MAT), mean temperature of the warmest month (MTWM), mean temperature of the coldest month, and mean annual precipitation (MAP) – based on HOF analyses (Huisman et al., 1993; Jansen and Oksanen, 2013).

Jouzel et al., 2007).

### 3.3. Reliability of the reconstruction results

We evaluate the reconstruction results from statistical, ecological, and climatological aspects. First, the plot of maximum abundance of taxa indicates that the modern data-set covers the range of taxon abundance in fossil samples of core ZB13-C2 well (Fig. 8), though Ranunculaceae and Asteraceae (non-*Artemisia*) are not so well covered. The differences, however, are within acceptable limits. The adequate coverage of the modern pollen samples helps to reduce the number of situations where there are no modern analogues for the fossil assemblages.

Second, analogue estimations based on a goodness-of-fit analysis indicate a good match between the fossil and modern pollen samples. 92.93%/6.89% of the fossil samples show a good or fair analogue quality (Fig. 9), while only five fossil samples (at 55 ka, 458 ka, 500.24 ka, 500.89 ka, 864.94 ka) have a poor-quality or lack of analogues (Fig. 9).

Third, bootstrap sample-specific estimates of standard error for each reconstructed value and the entire RMSEP are reasonable, mostly <1 °C (MAT: mean 0.46 °C; MMTWM: 0.39) and < 3.6 °C (MAT: mean 3.51 °C; MTWM: 4.06 °C) for both MAT and MTWM (Fig. 7; Fig. S10), further supporting that LW-WAPLS is an appropriate approach at the broad glacial-interglacial scale (Juggins and Birks, 2012). The sample-specific estimates of standard error cover, on average, 13% of the entire RMSEP, which is reasonable (Juggins and Birks, 2012). However, RMSEP could be overestimated for the LW-WAPLS approach, as large training-sets may include some inherent replication. When training-set size increases, leave-one-out RMSEP can become a less reliable estimate of true prediction error (Næs et al., 2002). LW-WAPLS uses 20 analogues for each fossil sample when doing WAPLS, which means that the reconstruction is independent of other fossil samples, possibly resulting in the RMSEP for the whole local training-set being over-estimated.

Fourth, a reconstruction significance test (Telford and Birks, 2011) results show that MTWM for the entire core explains more variance than 95% of all the random reconstructions, suggesting it is statistically significant. MAT shows similar variabilities to MTWM and is near the 95% significance line (Fig. 10), though it just fails to pass this test. However, palaeoSig does not test if the reconstructed values make sense climatically; it only tests if there is a statistically significant trend in the data relative to an ensemble of random reconstructions (Chevalier et al., 2020b). Climatically, the coherent change of MAT and MTWM over the past 1.74 Ma, similar to their relationship in modern climate (Figs. S2 and S11), supports the reliability of the MAT reconstruction. The MTCM reconstructions shows inconsistent changes with MAT and MTWM (Fig. S12 and Fig. 10) fails the significance test (Fig. 10). In this high-elevation region the vegetation almost stops growing, and the impact of MTCM could be minor considering that the conifer trees here can survive a very cold winter. Therefore the MTCM reconstruction could be largely biased. The precipitation reconstruction (MAP) shows muted changes (Fig. S12) and fails the significance test (Fig. 10), not surprisingly as it is not the major controller of the vegetation over the long time-scale. Nonetheless, the coherent variations in temperature, Rb/Sr, and carbonate%, which reflect the precipitation qualitatively, suggest coupled changes of temperature and precipitation over the past 1.74 Ma (Zhao et al., 2020).

In addition to these statistical evaluations, ecological considerations lend support to the reliability of the MAT and MTWM reconstructions (Fig. 11). *Picea*, *Betula,* and *Quercus* have high WA optima for both precipitation (550–750 mm) and temperature (MAT: 0.3–2.3 °C; MTWM: 10.6–11.5 °C). *Quercus* and *Betula* have even higher temperature and precipitation optima compared to *Picea*. The high pollen values of *Quercus*, *Betula,* and *Picea* during 1.74–1.54 Ma BP suggest warm conditions. In the interval of 1.74–1.54 Ma, *Artemisia* pollen has its highest abundances during glacial stages compared to other intervals in the core. *Artemisia* usually grows in arid and semi-arid regions but it favours warmer summers. The modern climate at the site is generally cool due to its high elevation. Only some cold-tolerant species can be found, for example *Artemisia frigida, A. roxburghiana, A. hedinii,* and *A. scoparia.,* on nearby mountains up to 3500–4000 m elevation. Prior to 1.54 Ma BP, the relatively higher summer temperature and the dry climate in the glacials may have allowed the expansion of *Artemisia*. Cyperaceae, Poaceae, and *Thalictrum* have lower MAT (∼ − 3 to −1 °C) and MTWM (∼9–10 °C) optima and relatively moderate MAP optima (∼450–550 mm) (Figs. 11 and 12). The reconstructed lower temperature in the last 0.62 Ma is also reflected by low pollen percentages of tree taxa.

Taxa with lower MAP optima (<450 mm), such as *Ephedra*, Chenopodiaceae, and *Nitraria* occupy a longer temperature gradient, and their abundances are mostly controlled by precipitation. However, these taxa are much less abundant (<2%) in the pollen assemblages in core ZB13-C2, and thus provide limited information about past precipitation conditions, which partly explains why the precipitation reconstruction fails the significance test (Fig. 10).

The long-term stepwise cooling appears to be consistent with the reconstructed biome changes (Fig. 2). At 1.74–1.54 and 1.54–1.03 Ma BP, the vegetation was dominated by forest. The period 1.74–1.54 Ma BP had more steppe intervals, while 1.54–1.03 Ma BP had more meadow and scrub intervals. The interval of 0.62–0 Ma BP had much less forest expansion, and the vegetation was mostly dominated by meadow and steppe. The 1.03–0.62 Ma BP interval is transitional with more frequent forest occurrence, but less than in the previous intervals.

Finally, from the climate viewpoint, the 4–5 °C glacial-interglacial range at Zoige for the interval 1.74–0.62 Ma BP, appears to be realistic considering the smaller glacial-interglacial difference globally and possibly with a small magnification on the high-latitude Tibetan Plateau. Over the past 0.62 Ma, a larger glacial-interglacial range than ∼4–5 °C is expected if one considers the overall global trend. Zhao et al. (2020) discuss that the emergence of longer and more extreme glacials in the last ∼0.62 Ma led to tree populations on the Tibetan Plateau seeking refugial locations at increasingly lower elevations. Longer migrational distances could then account for their subdued expansions, not only during glacials, but also during interglacials (Zhao et al., 2020). This tree migrational issue may have caused, to some degree, an underestimation of interglacial temperatures, which could explain why the inferred interglacial temperature at Zoige does not fit the global trends over the past 0.62 Ma.

Conifer forest in the Zoige region presently occurs between ∼3000–4000 m elevation, while desert mainly occurs above ∼4400 m (Fig. S1; Shen et al., 2005). The biggest elevational difference between the conifer forest and the desert belt is up to ∼1400 m, suggesting at most a ∼ 9 °C difference based on the existing lapse-rate temperature gradient (0.65 °C 100 $m^{-1}$). Considering the elevation of the coring site is 3434 m, the vegetation shift between conifer forest and steppe after 0.62 Ma BP should indicate a < ∼6.5 °C glacial-interglacial temperature difference. This assumption is supported by other palaeo-temperature records and simulations for the Tibetan Plateau. Neo-endemic ground beetles and private tree haplotypes reveal an LGM summer temperature depression of 3–4 °C for the southern Tibetan Plateau (Schmidt et al., 2011), which should have a smaller magnitude than the northern Tibetan Plateau. Thompson et al. (1989) estimated ∼6 °C last glaciation temperature depression based on $\delta^{18}O$ value from the Dunde ice-core on the northern Tibetan Plateau. Herzschuh et al. (2006) derived a ∼ 4.0–7.0 °C colder temperature during the LGM from the pollen record of a sediment core from the Qilian Mountains on the northeastern Plateau. GCM experiments show that the LGM surface temperatures are ∼4–7 °C lower than the current interglacial on the north-west and north-east Tibetan Plateau (Li et al., 2017).

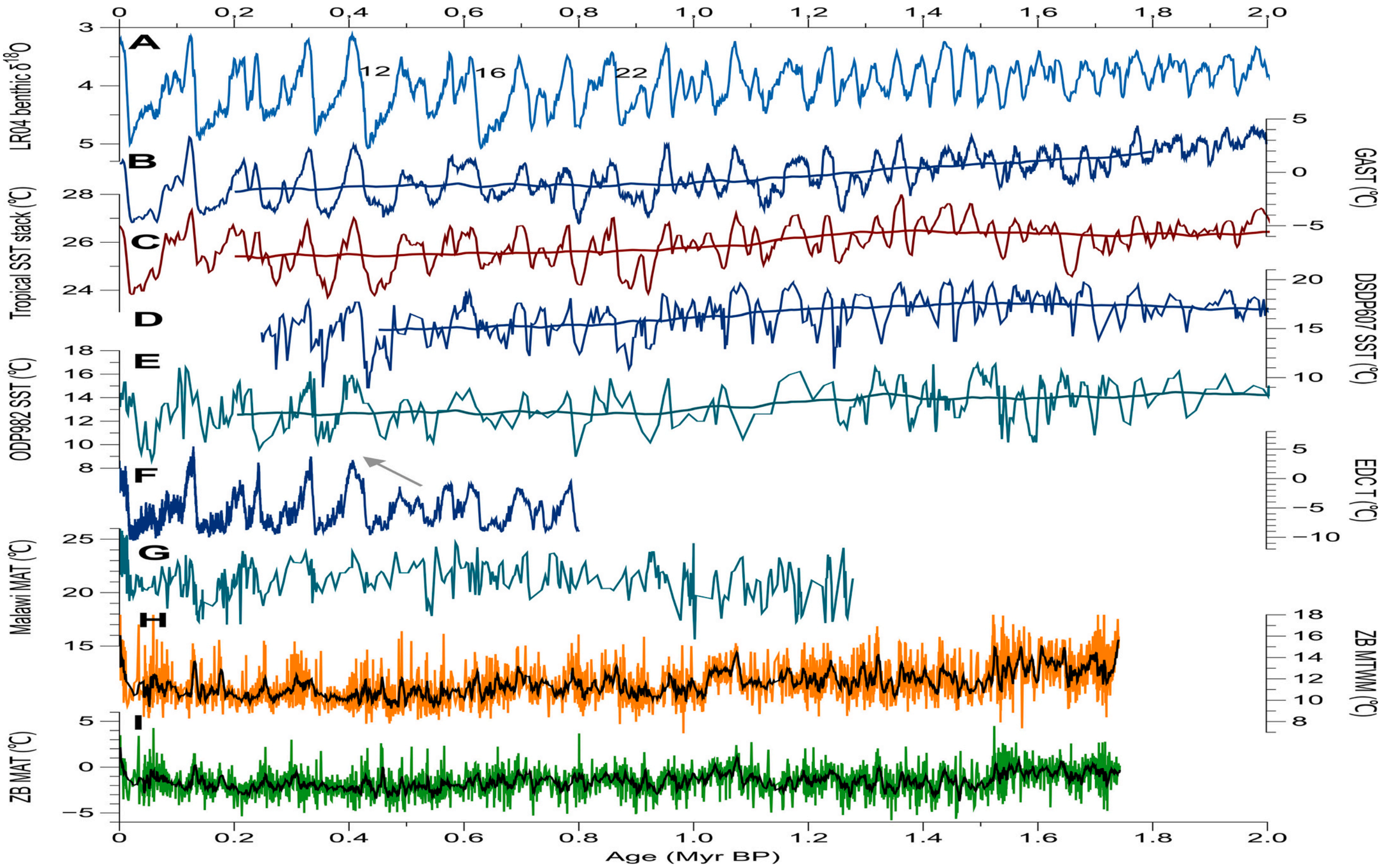


**Fig. 13.** Correlation of temperature records from the Zoige Basin core ZB13-C2 with global and regional climate records over the past 1.74 Ma. A. LR04 global benthic $\delta^{18}O$ stack (Lisiecki and Raymo, 2005). The numbers denote marine isotope stages. B. Global average surface temperature (GAST) as temperature deviation (°C) from present (average over 0–5 ka) (Snyder, 2016). C. Sea-surface temperature (SST) tropical stack (Herbert et al., 2010). D. Estimates of SST (°C) at deep-sea drilling project (DSDP) site 607 (Lawrence et al., 2010), in the north Atlantic. E. Estimates of SST (°C) at ocean drilling project (ODP) site 982 in the north Atlantic (Herbert et al., 2016). F. Stacked reconstruction of change in Antarctic temperature (°C) (Parrenin et al., 2013). G. $TEX_{86}$-based reconstructed temperature over the past 1.3 Ma from Lake Malawi (Johnson et al., 2016). H. Reconstructed mean temperature of the warmest month (MTWM) and 9-point running mean (black line) from ZB13-C2 (this study). I. Reconstructed mean annual temperature and 9-point running mean (black line) from ZB13-C2 (this study).

### 3.4. Comparisons with other regional temperature reconstructions

The reconstructed temperature for the Zoige Basin (ZB) shows a long-term cooling trend over the past 1.74 Ma, starting with warmer glacial and interglacial conditions, followed by the two biggest cooling steps at ~1.54 and ~ 0.62 Ma BP. These two cooling shifts are broadly consistent with the U1308 multi-proxy record that documents mode transitions at ~1.54 and 0.65 Ma (Hodell and Channell, 2016) (Fig. 13), which mark times of change in the growth of the Northern Hemisphere ice sheets. The Zoige record shows much higher glacial-stage temperatures before 1.54 Ma BP, suggesting smaller ice sheets during that interval (Hodell and Channell, 2016). The marked cooling during the glacials since 0.62 Ma onwards is consistent with the larger global ice-volume inferred from benthic $\delta^{18}O$ (Lisiecki and Raymo, 2005).

The comparisons between the general trend of temperature variabilities at Zoige and in the SST are discussed in Zhao et al. (2020). MAT and MTWM at Zoige mostly indicate ~4–5 °C and 5–6 °C glacial-interglacial ranges, respectively. They show a much larger range than tropical SST, which indicates <2.5–3 °C variabilities in most cases, except in MIS 24–22 and for the last 0.43 Ma with larger ranges (3–4 °C) (Herbert et al., 2010; Li et al., 2011; Fig. 13). Considering SST variations are muted compared to the larger terrestrial air temperature variabilities, the magnitude of the correlation appears robust. The MAT range at Zoige shows similarity to the SST of the North Atlantic, which mostly suggests 3–5 °C, but a 5–6 °C range after 0.43 Ma BP (Lawrence et al., 2010; Herbert et al., 2010), probably due to a magnification effect in high-latitude Atlantic regions.

Temperature reconstruction from the Antarctic ice-core Dome C indicates a ~ 8–9 °C glacial-interglacial range before 0.43 Ma BP. It shows cooler glacial and warmer interglacials since ~0.43 Ma BP, with a range of up to 12 °C. In lower latitude regions, the terrestrial record of $TEX_{86}$-based reconstructed temperature over the past 1.3 Ma from Lake Malawi shows a 2–4 °C range after 0.9 Ma BP, but a larger range (~4 °C) after 0.6 Ma BP (Johnson et al., 2016). Another coarse-resolution temperature reconstruction from a marine pollen record from Africa reveals an amplitude of ~4 °C range between glacial minima and interglacial maxima (Chevalier et al., 2020a). In the mid-latitude region, the 800-ka land-surface temperature (LST) reconstruction based on branched glycerol dialkyl glycerol tetraethers (brGDGT) records from two sections on the Loess Plateau shows a 4–10 °C range superimposed on the long-term cooling trend; however, it is different from air temperature, showing a much larger magnitude in variability (Lu et al., 2019). Surface vegetation or lack of vegetation are thought to have played an important role in regulating LSTs, superimposed on the fundamental global glacial–interglacial changes.

These comparisons reveal the range of gradients from high-, middle-, to low-latitude terrestrial regions (from ~8–9 °C, to ~4–5 °C and 2–4 °C), though all records show a cooling trend over long time-scales. The temperature variability at Zoige has a smaller range than the high-latitude regions, but larger than in the tropical regions. The Zoige temperature record provides valuable data for understanding the gradient of temperature variability over different latitudes at the glacial-interglacial scale, which is crucial for climate simulations.

## 4. Conclusions

A scarcity of high-quality continuous terrestrial quantitative paleoclimate records has greatly hampered our understanding of global and regional climate features on glacial-interglacial scales and of model simulations to elucidate the underlying mechanisms. We present a high-resolution pollen-based temperature reconstruction from the Zoige Basin on the eastern Tibetan Plateau using a new and robust approach, namely LW-WAPLS.

(1) Our results demonstrate that the newly developed LW-WAPLS approach is a potentially powerful tool for the quantitative reconstructions of climate on glacial-interglacial scales. Further LW-WAPLS studies based on more sites would be valuable.
(2) MAT and MTWM reconstructions at Zoige reveal the general stepwise cooling trend with two major shifts at 1.54 and 0.62 Ma BP. They indicate ~4–5 °C (MAT) and 5–6 °C (MTWM) glacial-interglacial ranges. From 0.62 Ma BP onwards, temperature during the interglacials is likely to be underestimated due to longer tree migrational distances.
(3) Our long-term temperature reconstruction fills a data gap in mid-latitude terrestrial regions and provides evidence for quantifying the magnitude of difference along latitudinal gradients over glacial-interglacial scales.

These results also provide important data for model simulations to elucidate the underlying mechanisms and further reveal the thermal effects of the Tibetan Plateau on the Asian monsoon.

Supplementary data to this article can be found online at https://doi.org/10.1016/j.gloplacha.2021.103433.

## Data and code availability

The modern climate data and modern pollen data ($n = 620$) from the first author's group) are included in Supplementary Table S1 and Table S2. The tree pollen percentages and reconstructed MAT and MTWM time-series are attached as Supplementary Table S3. The R code for climate data interpolation, climate reconstructions and other numerical analysis are listed in the Supplementary Text.

## Declaration of competing interest

The authors declare they have no conflict of interest.

## Acknowledgments

This research was supported by the National Key Research and Development Program of China (grant # 2016YFA 0600501), the National Natural Science Foundation of China (# 41888101, 41690113), and the Strategic Priority Research Program of the Chinese Academy of Sciences (#XDA20070101). HJBB and VAF are supported by the European Research Council Advanced Grant 741413 Humans on Plant Earth (HOPE) and VAF by the VISTA (Norwegian Academy of Science and Letters and Equinor) project IGNEX-eco (6166). We acknowledge discussions with Alistair Seddon, Richard Telford, Chronis Tzedakis and Jun Tian and practical help from Hilary Birks and Cathy Jenks. We gratefully acknowledge F. Marret-Davies and two anonymous reviewers for their constructive comments and useful suggestions.

## References

Abe, M., Hori, M., Yasunari, T., Kitoh, A., 2013. Effects of the Tibetan Plateau on the onset of the summer monsoon in South Asia: The role of the air-sea interaction. J. Geophys. Res: Atmospheres 118, 1760–1776.

An, Z.S., Clemens, S.C., Shen, J., Qiang, X.K., Jin, Z.D., Sun, Y.B., Prell, W.L., Luo, J.J., Wang, S.M., Xu, H., Cai, Y.J., Zhou, W.J., Liu, X.D., Liu, W.G., Shi, Z.G., Yan, L.B., Xiao, X.Y., Chang, H., Wu, F., Ai, L., Lu, F.Y., 2011. Glacial-interglacial Indian summer monsoon dynamics. Science 333, 719–723.

Birks, H.J.B., 1998. Numerical techniques in palaeolimnology – progress, potentialities, and problems. J. Paleolimnol. 20, 307–331.

Birks, H.J.B., 2012. Overview of numerical methods in palaeolimnology. In: Birks, H.J.B., Lotter, A.F., Juggins, S., Smol, J.P. (Eds.), Tracking Environmental Change Using Lake Sediments Vol. 5: Data Handling and Numerical Techniques. Springer Dordrecht, Dordrecht, pp. 19–92.

Birks, H.J.B., Simpson, G.L., 2013. 'Diatoms and pH reconstruction' (1990) revisited. J. Paleolimnol. 49, 363–371.

Birks, H.J.B., Line, J.M., Juggins, S., Stevenson, A.C., ter Braak, C.J.F., 1990a. Diatoms and pH reconstruction. Philos. Trans. R. Soc. Lond. B 327, 263–278.

Birks, H.J.B., Juggins, S., Line, J.M., 1990b. Lake surface water chemistry reconstructions from palaeolimnological data. In: Mason, B.J. (Ed.), The Surface Water Acidification Programme. Cambridge University Press, Cambridge, pp. 301–313.

Birks, H.J.B., Heiri, O., Seppä, H., Bjune, A.E., 2010. Strengths and weaknesses of quantitative climate reconstructions based on late-quaternary biological proxies. Open Ecol. J. 3, 68–110.
Brigham-Grette, J., Melles, M., Minyuk, P., Andreev, A., Tarasov, P., DeConto, R., Koenig, S., Nowaczyk, N., Wennrich, V., Rosén, P., Haltia, E., Cook, T., Gebhardt, C., Meyer-Jacob, C., Snyder, J., Herzschuh, U., 2013. Pliocene Warmth, polar amplification, and stepped pleistocene cooling recorded in NE Arctic Russia. Science 340, 1421–1427.
Cao, X.Y., Herzschuh, U., Ni, J., Zhao, Y., Boehmer, T., 2014. Spatial and temporal distributions of major tree taxa in eastern continental Asia during the last 22,000 yr. The Holocene 25, 79–91.
Cao, X., Tian, F., Telford, R.J., Ni, J., Xu, Q., Chen, F., Liu, X., Stebich, M., Zhao, Y., Herzschuh, U., 2017. Impacts of the spatial extent of pollen-climate calibration-set on the absolute values, range and trends of reconstructed Holocene precipitation. Quat. Sci. Rev. 178, 37–53.
Chen, F.H., Bloemendal, J., Zhang, P.Z., Liu, G.X., 1999. An 800 ky proxy record of climate from lake sediments of the Zoige Basin, eastern Tibetan Plateau. Palaeogeogr. Palaeoclimatol. Palaeoecol. 151, 307–320.
Chevalier, M., Chase, B.M., Quick, L.J., Dupont, L.M., Johnson, T.C., 2020a. Temperature change in subtropical southeastern Africa during the past 790,000 yr. Geology. https://doi.org/10.1130/G47841.1.
Chevalier, M., Davis, B.A.S., Heiri, O., Seppä, H., Chase, B.M., Gajewski, K., Lacourse, T., Telford, R.J., Finsinger, W., Guiot, J., Kühl, N., Maezumi, S.Y., Tipton, J.R., Carter, V.A., Brussel, T., Phelps, L.N., Dawson, A., Zanon, M., Vallé, F., Nolan, C., Mauri, A., de Vernal, A., Izumi, K., Holmström, L., Marsicek, J., Goring, S., Sommer, P.S., Chaput, M., Kupriyanov, D., 2020b. Pollen-based climate reconstruction techniques for late Quaternary studies. Earth Sci. Rev. 210, 103384.
Dallmeyer, A., Claussen, M., Herzschuh, U., Fischer, N., 2011. Holocene vegetation and biomass changes on the Tibetan Plateau - a model-pollen data comparison. Clim. Past 7, 881–901.
Ding, Z.L., Derbyshire, E., Yang, S.L., Yu, Z.W., Xiong, S.F., Liu, T.S., 2002. Stacked 2.6-Ma grain size record from the Chinese loess based on five sections and correlation with the deep sea δ18O record. Paleoceanography 17, 1–21.
Gilbert, P., Varadhan, R., 2019. NumDeriv: Accurate Numerical Derivatives. R. package version 2016.8-1.1. https://CRAN.R-project.org/package=numDeriv.
Guiot, J., 1990. Methodology of the last climatic cycle reconstruction in France from pollen data. Palaeogeogr. Palaeoclimatol. Palaeoecol. 80, 49–69.
Guo, Z.T., Biscaye, P., Wei, L.Y., Chen, X.H., Peng, S.Z., Liu, T.S., 2000. Summer monsoon variations over the last 1.2 Ma from the weathering of loess-soil sequences in China. Geophys. Res. Lett. 27, 1751–1754.
Guiot, J., Torre, F., Jolly, D., Peyron, O., Boreux, J.J., Cheddadi, R., 2000. Inverse vegetation modeling by Monte Carlo sampling to reconstruct palaeoclimates under changed precipitation seasonality and CO2 conditions: Application to glacial climate in Mediterranean region. Ecol. Model. 127 (2–3), 119–140.
Guo, Z.T., Ruddiman, W.F., Hao, Q.Z., Wu, H.B., Qiao, Y.S., Zhu, R.X., Peng, S.Z., Wei, J.J., Yuan, B.Y., Liu, T.S., 2002. Onset of Asian desertification by 22 Myr ago inferred from loess deposits in China. Nature 416, 159–163.
Haslett, J., Whiley, M., Bhattacharya, S., Salter-Townshend, M., Wilson, S.P., Allen, J.R.M., Huntley, B., Mitchell, F.J.G., 2006. Bayesian palaeoclimate reconstruction. J. R. Stat. Soc. Ser. A 169, 395–438.
Herbert, T.D., Peterson, L.C., Lawrence, K.T., Liu, Z.H., 2010. Tropical ocean temperatures over the past 3.5 million years. Science 328, 1530–1534.
Herzschuh, U., Kürschner, H., Mischke, S., 2006. Temperature variability and vertical vegetation belt shifts during the last ~50,000 yr in the Qilian Mountains (NE margin of the Tibetan Plateau, China). Quat. Res. 66, 133–146.
Herzschuh, U., Ni, J., Birks, H.J.B., Böhnerf, J., 2011. Driving forces of mid-Holocene vegetation shifts on the upper Tibetan Plateau, with emphasis on changes in atmospheric $CO_2$ concentrations. Quat. Sci. Rev. 30, 1907–1917.
Herzschuh, U., Cao, X.Y., Laepple, T., Dallmeyer, A., Telford, R.J., Ni, J., Chen, F.H., Kong, Z.C., Liu, G.X., Liu, K.-B., Liu, X.Q., Stebich, M., Tang, L.Y., Tian, F., Wang, Y. B., Wischnewski, J., Xu, Q.H., Yan, S., Yang, Z.J., Yu, G., Zhang, Y., Zhao, Y., Zheng, Z., 2019. Position and orientation of the westerly jet determined Holocene rainfall patterns in China. Nat. Commun. 10, 2376–2383.
Hijmans, R.J., Cameron, S.E., Parra, J.L., Jones, P.G., Jarvis, A., 2005. Very high resolution interpolated climate surfaces for global land areas. Int. J. Climatol. 25, 1965–1978.
Hodell, D.A., Channell, J.E.T., 2016. Mode transitions in Northern Hemisphere glaciation: co-evolution of millennial and orbital variability in Quaternary climate. Clim. Past 12, 1805–1828.
Holden, P.B., Birks, H.J.B., Brooks, S.J., Bush, M.B., Hwang, G.M., Matthews-Bird, F., Valencia, B.G., van Woesik, R., 2017. BUMPER v1.0: a Bayesian user-friendly model for palaeo-environmental reconstruction. Geosci. Model Dev. 10, 483–498.
Hou, X.Y., 2001. Vegetation Atlas of China (Scale: 1:1,000,000) I-48. Science Press, Beijing.
Hubener, T., Dressler, M., Schwarz, A., Langner, K., Adler, S., 2008. Dynamic adjustment of training-sets ('moving-window' reconstruction) by using transfer functions in paleolimnology – a new approach. J. Paleolimnol. 40, 79–95.
Huisman, J., Olff, H., Fresco, L.F.M., 1993. A hierarchical set of models for species response analysis. J. Veg. Sci. 4, 37–46.
Izumi, K., Bartlein, P.J., 2016. North American paleoclimate reconstructions for the Last Glacial Maximum using an inverse modeling through iterative forward modeling approach applied to pollen data. Geophys. Res. Lett. 43, 10,965–10,972.
Jansen, F., Oksanen, J., 2013. How to model species responses along ecological gradients – Huisman-Olff-Fresco models revisited. J. Veg. Sci. 24, 1108–1117.
Johnson, T.C., Werne, J.P., Brown, E.T., Abbott, A., Berke, M., Steinman, B.A., Halbur, J., Contreras, S., Grosshuesch, S., Deino, A., Scholz, C.A., Lyons, R.P., Schouten, S., Damsté, J.S.S., 2016. A progressively wetter climate in southern East Africa over the past 1.3 million years. Nature 537, 220–224.
Jouzel, J., Masson-Delmotte, V., Cattani, O., Dreyfus, G., Falourd, S., Hoffmann, G., Minster, B., Nouet, J., Barnola, J.M., Chappellaz, J., Fischer, H., Gallet, J.C., Johnsen, S., Leuenberger, M., Loulergue, L., Luethi, D., Oerter, H., Parrenin, F., Raisbeck, G., Raynaud, D., Schilt, A., Schwander, J., Selmo, E., Souchez, R., Spahni, R., Stauffer, B., Steffensen, J.P., Stenni, B., Stocker, T.F., Tison, J.L., Werner, M., Wolff, E.W., 2007. Orbital and Millennial Antarctic climate variability over the past 800,000 years. Science 317, 793–796.
Juggins, S., 2013. Quantitative reconstructions in palaeolimnology: new paradigm or sick science? Quat. Sci. Rev. 64, 20–32.
Juggins, S., 2017. Rioja: Analysis of Quaternary Science Data. R package version 0.9-21. http://cran.r-project.org/package=rioja.
Juggins, S., Birks, H.J.B., 2012. Quantitative enviornmental reconstructions from biological data. In: Birks, H.J.B., Lotter, A.F., Juggins, S., Smol, J.P. (Eds.), Tracking Environmental Change Using Lake Sediments vol. 5: Data Handling and Numerical Techniques. Springer Netherlands, Dordrecht, pp. 431–494.
Kühl, N., Gebhardt, C., Litt, T., Hense, A., 2002. Probability density functions as botanical-climatological transfer functions for climate reconstruction. Quat. Res. 58, 381–392.
Kühl, N., Litt, T., Schölzel, C., Hense, A., 2007. Eemian and early Weichselian temperature and precipitation variability in northern Germany. Quat. Sci. Rev. 26, 3311–3317.
Lawrence, K.T., Sosdian, S., White, H.E., Rosenthal, Y., 2010. North Atlantic climate evolution through the Plio-Pleistocene climate transitions. Earth Planet. Sci. Lett. 300, 329–342.
Li, L., Li, Q.Y., Tian, J., Wang, P.X., Wang, H., Liu, Z.H., 2011. A 4-Ma record of thermal evolution in the tropical western Pacific and its implications on climate change. Earth Planet. Sci. Lett. 309, 10–20.
Li, J.M., Ehlers, T.A., Werner, M., Mutz, S.G., Steger, C., Paeth, H., 2017. Late Quaternary climate, precipitation $\delta^{18}O$, and Indian monsoon variations over the Tibetan Plateau. Earth Planet. Sci. Lett. 457, 412–422.
Liang, C., Zhao, Y., Qin, F., Zheng, Z., Xiao, X.Y., Ma, C.M., Li, H., Zhao, W.W., 2020. Pollen-based Holocene quantitative temperature reconstruction on the eastern Tibetan Plateau using a comprehensive method framework. Sci. China Earth Sci. 63 (8), 1144–1160.
Lisiecki, L.E., Raymo, M.E., 2005. A Pliocene-Pleistocene stack of 57 globally distributed benthic $\delta^{18}O$ records. Paleoceanography 20, 1–17.
Lu, H., Wu, N., Liu, K.-B., Zhu, L., Yang, S., Yao, T., Wang, L., Li, Q., Liu, X., Shen, C., Li, X., Tong, G., Jiang, H., 2011. Modern pollen distributions in Qinghai-Tibetan Plateau and the development of transfer functions for reconstructing Holocene environmental changes. Quat. Sci. Rev. 30, 947–966.
Lu, H.X., Liu, W.G., Yang, H., Wang, H.Y., Liu, Z.H., Leng, Q., Sun, Y.B., Zhou, W.J., An, Z.S., 2019. 800-kyr land temperature variations modulated by vegetation changes on Chinese Loess Plateau. Nat. Commun. 10, 1958.
Marchetto, A., 1994. Rescaling species optima by weighted averaging. J. Paleolimnol. 12, 155–163.
Melles, M., Brigham-Grette, J., Minyuk, P.S., Nowaczyk, N.R., Wennrich, V., DeConto, R. M., Anderson, P.M., Andreev, A.A., Coletti, A., Cook, T.L., Haltia-Hovi, E., Kukkonen, M., Lozhkin, A.V., Rosén, P., Tarasov, P., Vogel, H., Wagner, B., 2012. 2.8 million years of Arctic climate change from Lake El'gygytgyn, NE Russia. Science 337, 315–320.
Næs, T., Isaksson, T., Fearn, T., Davies, T., 2002. A User-Friendly Guide to Multivariate Calibration and Classification. NIR Publications, Chichester.
Nychka, D., Furrer, R., Paige, J., Sain, S., Gerber, F., Iverson, M., 2020. Fields: Tool for Spatial Data. https://CRAN.R-project.org/package=fields.
Oksanen, J., Blanchet, F.G., Friendly, M., Kindt, R., Legendre, P., McGlinn, D., Minchin, P.R., O'Hara, R.B., Simpson, G.L., Solymos, P., Stevens, M.H.H., Szoecs, E., Wagner, H., 2019. Community Ecology Package. R package version 2.5-6. https://CRAN.R-project.org/package=vegan.
Overpeck, J.T., Webb, T., Prentice, I.C., 1985. Quantitative interpretation of fossil pollen spectra: Dissimilarity coefficients and the method of modern analogs. Quat. Res. 23, 87–108.
Parrenin, F., Masson-Delmotte, V., Köhler, P., Raynaud, D., Paillard, D., Schwander, J., Barbante, C., Landais, A., Wegner, A., Jouzel, J., 2013. Synchronous change of atmospheric $CO_2$ and Antarctic temperature during the last Deglacial Warming. Science 339, 1060–1063.
Petit, J.R., Jouzel, J., Raynaud, D., Barkov, N.I., Barnola, J.M., Basile, I., Bender, M., Chappellaz, J., Davis, M., Delaygue, G., Delmotte, M., Kotlyakov, V.M., Legrand, M., Lipenkov, V.Y., Lorius, C., Pepin, L., Ritz, C., Saltzman, E., Stievenard, M., 1999. Climate and atmospheric history of the past 420,000 years from the Vostok ice core, Antarctica. Nature 399, 429–436.
Polley, H.W., Johnson, H.B., Marino, B., Mayeux, H.S., 1993. Increase in C3 plant water-use efficiency and biomass over Glacial to present $CO_2$ concentrations. Nature 361, 61–64.
Prentice, I.C., Harrison, S.P., 2009. Ecosystem effects of CO2 concentration: evidence from past climates. Clim. Past 5, 297–307.
Prokopenko, A.A., Hinnov, L.A., Williams, D.F., Kuzmin, M.I., 2006. Orbital forcing of continental climate during the Pleistocene: a complete astronomically tuned climatic record from Lake Baikal, SE Siberia. Quat. Sci. Rev. 25, 3431–3457.
R Core Team, 2019. R: A Language and Environment for Statistical Computing. R for Statistical Computing, Vienna. https://www.R-Project.org.
Schmidt, J., Opgenoorth, L., Martens, J., Miehe, G., 2011. Neoendemic ground beetles and private tree haplotypes: two independent proxies attest a moderate last glacial maximum summer temperature depression of 3-4 °C for the southern Tibetan Plateau. Quat. Sci. Rev. 30, 1918–1925.

Shen, C.M., Tang, L.Y., Wang, S.M., Li, C.H., Liu, K.B., 2005. Pollen records and time scale for the RM core of the Zoige Basin, northeastern Qinghai-Tibetan Plateau. Chin. Sci. Bull. 50, 553–562.
Simpson, G.L., 2012. Analogue methods in palaeolimnology. In: HJB, Birks, Lotter, A.F., Juggins, S., Smol, J.P. (Eds.), Tracking Environmental Change Using Lake Sediments. Volume 5: Data Handling and Numerical Techniques. Springer, Dordrecht, pp. 495–538.
Simpson, G.L., 2018. Modelling palaeoecological time series using generalised additive models. Front. Ecol. Evol. 6, 149. https://doi.org/10.3389/fevo.2018.00149.
Simpson, G.L., Oksanen, J., 2020. Analogue: Analogue matching and Modern Analogue Technique Transfer Function Models. R package version 0.17-4. https://cran.r-project.org/package=analogue.
Snyder, C.W., 2016. Evolution of global temperature over the past two million years. Nature 538, 226–228.
Telford, R.J., 2019. palaeoSig: Significance Tests of Quantitative Palaeoenvironmental Reconstructions. R package version 2.0-3. http://cran.r-project.org/package=palaeoSig.
Telford, R.J., Birks, H.J.B., 2005. The secret assumption of transfer functions: problems with spatial autocorrelation in evaluating model performance. Quat. Sci. Rev. 24, 2173–2179.
Telford, R.J., Birks, H.J.B., 2011. A novel method for assessing the statistical significance of quantitative reconstructions inferred from biotic assemblages. Quat. Sci. Rev. 30, 1272–1278.
Ter Braak, C.J.F., 1988. CANOCO-a FORTRAN Program for Canonical Community Ordination by [Partial] [Detrended] [Canonical] Correspondence Analysis, Principal Components Analysis and Redundancy Analysis Version 2.1. Agricultural Mathematics Group, Wageningen, The Netherlands.
Ter Braak, C.J.F., 1994. Canonical community ordination. Part I: Basic theory and linear methods. Ecoscience 1, 127–140.
Ter Braak, C.J.F., Juggins, S., 1993. Weighted averaging partial least squares regression (WA-PLS): an improved method for reconstructing environmental variables from species assemblages. Hydrobiologica 269/279, 485.202.
Ter Braak, C.J.F., Verdonschot, P.F.M., 1995. Canonical correspondence analysis and related multivariate methods in aquatic ecology. Aquat. Sci. 57, 255–289.
Therneau, T.M., Beth Atkinson, B., 2014. Mvpart: Multivariate Regression Trees. https://CRAN.R-project.org/package=mvpart.
Thompson, L.G., Mosley-Thompson, E., Davis, M.E., Bolzan, J.F., Klein, L., Yao, T.D., Wu, X., Xie, Z., Gundestrup, N., 1989. Holocene late pleistocene climatic ice core records from Qinghai - Tibetan plateau. Science 246, 474–477.
Torres, V., Hooghiemstra, H., Lourens, L., Tzedakis, P.C., 2013. Astronomical tuning of long pollen records reveals the dynamic history of montane biomes and lake levels in the tropical high Andes during the Quaternary. Quat. Sci. Rev. 63, 59–72.
Tzedakis, P.C., Hooghiemstra, H., Pälike, H., 2006. The last 1.35 million years at Tenaghi Philippon: revised chronostratigraphy and long-term vegetation trends. Quat. Sci. Rev. 25, 3416–3430.
Wagner, B., Vogel, H., Francke, A., Friedrich, T., Donders, T., Lacey, J.H., Leng, M.J., Regattieri, E., Sadori, L., Wilke, T., Zanchetta, G., Albrecht, C., Bertini, A., Combourieu-Nebout, N., Cvetkoska, A., Giaccio, B., Grazhdani, A., Hauffe, T., Holtvoeth, J., Joannin, S., Jovanovska, E., Just, J., Kouli, K., Kousis, I., Koutsodendris, A., Krastel, S., Lagos, M., Leicher, N., Levkov, Z., Lindhorst, K., Masi, A., Melles, M., Mercuri, A.M., Nomade, S., Nowaczyk, N., Panagiotopoulos, K., Peyron, O., Reed, J.M., Sagnotti, L., Sinopoli, G., Stelbrink, B., Sulpizio, R., Timmermann, A., Tofilovska, S., Torri, P., Wagner-Cremer, F., Wonik, T., Zhang, X. S., 2019. Mediterranean winter rainfall in phase with African monsoons during the past 1.36 million years. Nature 573, 256–260.
Webb, T., Bryson, R.A., 1972. Late- and post-glacial climate change in Northern Midwest, USA: quantitative estimates derived from fossil pollen spectra by multivariate statistical analysis. Quat. Res. 2, 70–115.
Wood, S.N., 2017. Generalized Additive Models: An Introduction with R, (2nd ed.). Chapman and Hall//CRC.
Wu, H., Guiot, J., Brewer, S.C., Guo, Z.T., 2007a. Climatic changes in Eurasia and Africa at the last glacial maximum and mid-Holocene: reconstruction from pollen data using inverse vegetation modelling. Clim. Dyn. 29, 211–229.
Wu, H., Guiot, J., Brewer, S., Guo, Z., Peng, C., 2007b. Dominant factors controlling glacial and interglacial variations in the tree line elevation in tropical Africa. Proc. Natl. Acad. Sci. U.S.A. 104, 9720–9724.
Wu, G.X., Liu, Y.M., Mao, J.Y., Ren, R.C., Bao, Q., He, B., Liu, B.Q., Hu, W.T., 2015. Tibetan Plateau climate dynamics: recent research progress and outlook. Natl. Sci. Rev. 2, 100–116.
Yee, T.W., Mitchell, N.D., 1991. Generalised additive models in plant ecology. J. Veg. Sci. 2, 587–602.
Zhao, Y., Yu, Z.C., Zhao, W.W., 2011. Holocene vegetation and climate histories in the eastern Tibetan Plateau: controls by insolation-driven temperature or monsoon-derived precipitation changes? Quat. Sci. Rev. 30, 1173–1184.
Zhao, Y., Tzedakis, P.C., Li, Q., Qin, F., Cui, Q.Y., Liang, C., Birks, H.J.B., Liu, Y.L., Zhang, Z.Y., Ge, J.Y., Zhao, H., Frelde, V.A., Deng, C.L., Cai, M.t., Li, H., Ren, W.H., Wei, H.C., Yang, H.F., Zhang, J.W., Yu, Z.C., Guo, Z.T., 2020. Evolution of vegetation and climate variability on the Tibetan Plateau over the past 1.74 Myr. Sci. Adv. https://doi.org/10.1126/sciadv.aay6193.
Zheng, Z., Huang, K.Y., Xu, Q.H., Lu, H.Y., Cheddadi, R., Luo, Y.L., Beaudouin, C., Luo, C. X., Zheng, Y.W., Li, C.H., Wei, J.H., Du, C.B., 2008. Comparison of climatic threshold of geographical distribution between dominant plants and surface pollen in China. Sci. China Ser. D Earth Sci. 51, 1107–1120.